Molecular Beam Epitaxy and Characterization of Doped Topological Insulators for Spintronics and Quantum Anomalous Hall Effect Applications

by

AHMAD EL ZATARI

A Dissertation Submitted to the
Graduate School of Sciences and Engineering
in Partial Fulfillment of the Requirements for
the Degree of

Master of Science

in

Electrical and Electronics Engineering

September 19, 2024

Molecular Beam Epitaxy and Characterization of Doped Topological Insulators for Spintronics and Quantum Anomalous Hall Effect Applications

Koç University

Graduate School of Sciences and Engineering

This is to certify that I have examined this copy of a master's thesis by

AHMAD EL ZATARI

and have found that it is complete and satisfactory in all respects,
and that any and all revisions required by the final
examining committee have been made.

Committee Members:

Assoc. Prof. Dr. Mehmet Cengiz Onbaşlı (Advisor)

Assist. Prof. Dr. Murat Kuşçu

Assoc. Prof. Dr. Murat Kaya Yapıcı

Date: _____

I dedicate this thesis to my family and friends.

ABSTRACT

Molecular Beam Epitaxy and Characterization of Doped Topological Insulators for Spintronics and Quantum Anomalous Hall Effect Applications

Master of Science in Electrical and Electronics Engineering

September 19, 2024

Topological insulators are highly valued for their distinctive electronic properties, particularly their topologically protected surface states. Among TIs, Bi_2Te_3 stands out due to its large bulk band gap. The realization of topologically protected surface states is largely dependent on the quality of deposited thin films. However, the epitaxial growth modes, thickness, and phase segregation of Bi_2Te_3 and its Sb-doped variant remain inadequately understood.

Our study aims to elucidate the effects and importance of growth kinetics on the quality of thin films deposited, including deposition rates, annealing time, substrate temperature, and growth duration. We employed techniques such as X-ray diffraction, X-ray reflectivity, and atomic force microscopy for structural characterization, X-ray photoelectron spectroscopy and energy-dispersive X-ray spectroscopy for electronic characterization, and Raman spectroscopy for optical characterization.

We explored two main avenues. First, we investigated the impact of growth rate on strain in Bi_2Te_3 thin films by varying the flux of deposited material. Second, we examined the effect of doping levels in Sb-doped Bi_2Te_3. In both investigations, all other growth parameters were kept constant.

In our analysis we observed an undesirable secondary phase peak at 015 in both Bi_2Te_3 and Sb-doped Bi_2Te_3 films. For Bi_2Te_3 films, reducing the growth rate nearly eliminated this secondary phase. In Sb-doped Bi_2Te_3, increasing the Sb flux achieved a similar result. In both cases, pronounced thickness fringes indicated coherence between the film surface and the substrate. Our research underlines the capability of our deposition system to achieve high-quality growth and fine-tuned control over the properties of Bi_2Te_3 and its Sb-doped films, demonstrating significant potential for future electronic and spintronic applications.

ÖZETÇE

Spintronik ve Kuantum Anomal Hall Etkisi Uygulamaları için Katkılı Topolojik Yalıtkanların Moleküler Demet Epitaksisi ve Karakterizasyonu

Elektrik-Elektronik Mühendisliği Yüksek Lisansı

19 Eylül 2024

Topolojik yalıtkanlar (TY), özellikle topolojik olarak korunan yüzey durumları nedeniyle, benzersiz elektronik özellikleri açısından büyük değer taşımaktadır. TY'lar arasında Bi_2Te_3, geniş hacim bant aralığı nedeniyle öne çıkmaktadır. Topolojik olarak korunan yüzey durumlarının gerçekleştirilmesi, büyük ölçüde biriktirilen ince filmlerin kalitesine bağlıdır. Bununla birlikte, Bi_2Te_3 ve Sb katkılı varyantının epitaksiyel büyüme modları, kalınlığı ve faz ayrışması yeterince anlaşılmamıştır.

Bu çalışmamız, biriktirme hızları, tavlama süresi, alttaş sıcaklığı ve büyüme süresi dahil olmak üzere büyüme kinetiğinin biriktirilen ince filmlerin kalitesi üzerindeki etkilerini ve önemini açıklamayı amaçlamaktadır. Yapısal karakterizasyon için X-ışını kırınımı, X-ışını yansıması ve atomik kuvvet mikroskopu; elektronik karakterizasyon için X-ışını fotoelektron spektroskopisi ve enerji dağılımlı X-ışını spektroskopisi ve optik karakterizasyon için Raman spektroskopisi tekniklerini kullanılmıştır.

Bu tez çalışmasında iki ana yol izlenmiştir. İlk olarak, biriktirilen malzemenin akışı değiştirilerek Bi_2Te_3 ince filmlerinin kalınlığının filmlerdeki gerilme üzerindeki etkisi araştırılmıştır. İkinci olarak, Sb katkılı Bi_2Te_3'de katkılama seviyelerinin yapısal özelliklere etkisi incelenmiştir. Her iki alt çalışmada da diğer tüm büyütme parametreleri sabit tutulmuştur.

Analizimizde hem Bi_2Te_3 hem de Sb katkılı Bi_2Te_3 filmlerinde 015'te istenmeyen bir ikincil faz piki gözlemlenmiştir. Bi_2Te_3 filmleri için büyüme hızının azaltılması bu ikincil fazı neredeyse ortadan kaldırmıştır. Sb katkılı Bi_2Te_3'de, Sb akışının artırılması benzer bir sonuç getirmiştir. Her iki durumda da belirgin kalınlık saçakları film yüzeyi ile substrat arasındaki uyumu göstermiştir. Araştırmamız, biriktirme sistemimizin yüksek kaliteli büyüme ve Bi_2Te_3 ile Sb katkılı filmlerinin özelliklerinin ince ayarlanmış kontrolünü sağlama yeteneğini vurgulamakta ve gelecekteki elektronik ve spintronik uygulamalar için önemli bir potansiyel göstermektedir.

ACKNOWLEDGEMENTS

I would like to immensely acknowledge my advisor, Assoc. Prof. Dr. Mehmet Cengiz Onbaşlı, for all the guidance and support he provided me in my masters journey. After I had a mini-heart attack in my first semester, my advisor made sure my health came first and supported in all ways possible. His knowledge and compasion helped me immensely in shaping my research expertise.

I would like to acknowledge Dr. Ferhat Katmis for the technical teaching he gave me on the PLD, MBE and sputtering chamber amongst other things he supported me with.

I would also like to extend my sincere appreciation and gratitude especially to my mother, father, brother, and sister, Sarwat, Zaki, Mohsen, and Hala, and my close friend, Omer for their continuous support and love throughout the years. I would not have made it to where I am now without their support.

I would also like to extend my gratitude to my colleagues, Ebrahim Zahrabi, Aykut Can Onel, Rawana Yagan, Roya Kavkhani, Arooba Maryam, and Kerem Anar for all the help and assistance they provided.

Lastly, I would like to gratefully acknowledge the European Research Council (ERC) Starting Grant SKYNOLIMIT (“Ultralow power and ultra-wideband spintronics near thermodynamic limits”) with No. 948063, the ERC Proof of Concept project SuperPHOTON (“2D Topological Superconducting Single Photon Detector Devices”) with No. 101100718, and TÜBİTAK 1001 project no. 120F230.

To everyone mentioned and everyone not mentioned, I want to thank you from the bottom of my heart for all the support during my journey.

TABLE OF CONTENTS

LIST OF TABLES

LIST OF FIGURES

ABBREVIATIONS

2D	two dimensional
AFM	Dynamic Programming
AREPS	Angle-Resolved Photoemission Spectroscopy
BCB	Bulk Conduction Band
Bi	Bismuth
Bi_2Se3	Bismuth Selenide
Bi_2Te_3	Bismuth Telluride
DP	Dirac Point
EF	Fermi level
MBE	Molecular Beam Epitaxy
PLD	Pulsed Laser Deposition
QL	Quintuple Layer
QAHE	Quantum Anomalous Hall Effect
RHEED	Reflection High Energy Electron Diffraction
Sb	Antimony
Si	Silicon
STM	Scanning tunnelling microscopy
TCI	Topological Crystalline Insulator
Te	Tellurium
TI	Topological Insulator
TRS	Time Reversal Symmetry
UHV	Ultra-High Vacuum
W	Tungsten
XRD	X-ray Diffraction
XRR	X-ray reflectivity

Chapter 1:
INTRODUCTION

1.1 Background and Motivation

Topological insulators (TI) are materials with insulating bulk properties and conducting surface states that are topologically protected with Dirac-like band structure. The formation of such states at the surface or edges with energies that cross the Fermi level (E_F) is Due to the non-trivial topology of the bulk band structure. These surface states exhibit unique electronic properties such as spin momentum locking, robustness against impurities and imperfections, and protection against back scattering[1-8]. Due to this nature of TIs, the band gap can be controlled using multiple ways such as doping, strain inducing or application of external fields[2,4,7,9,10]. The Dirac cone refers to the dispersion relation of the topologically protected surface states[3,4,8,11,12]. These surface states form two cone-like structures that meet at a single point near the E_F in the momentum space known as the Dirac point (DP). Figure 1.1 shows the effect of Antimony (Sb) doping of Bismuth Telluride (Bi_2Te_3) on the E_F energy which in turn shows the effect on the DP position in the band gap. The band inversion due to the strong spin orbit coupling results in the formation of the Dirac cone. The Dirac cone can be modulated by tuning the stoichiometry. Tuning of the TIs content makes it possible to control the energy level of the DP in the band gap and the sign of the Dirac carriers[4]. Dirac cones can also be tuned by crystalline strain. Strain in the vicinity of grain boundaries can cause enhancement or destruction of the surface states[2].

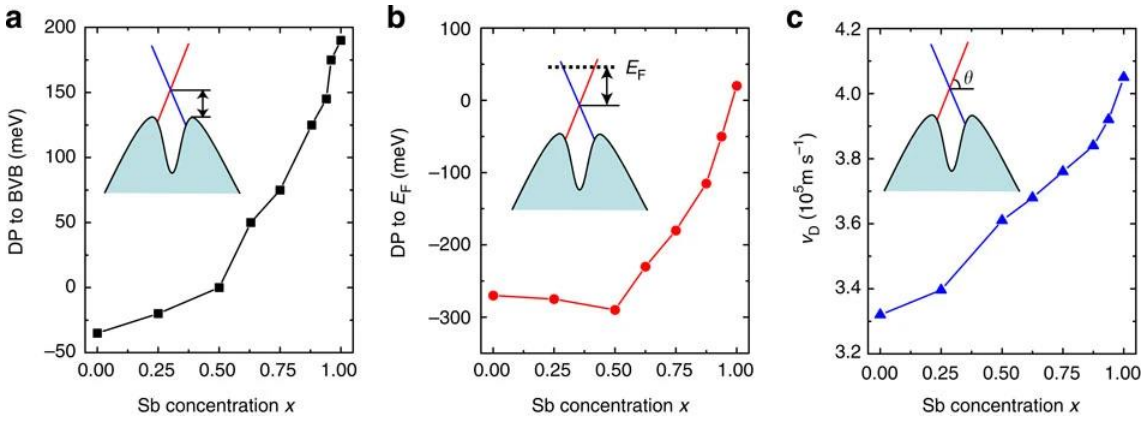

*Figure 1.1: (**a**) Relative position between the DP and the top of BVB near the Γ point[8]. (**b**) Relative position between the DP and the E_F[8]. (**c**) The Dirac fermion velocity v_D (v_D ~tanθ) extracted from the linear dispersion near the DP. All three quantities evolve smoothly from that of pure Bi_2Te_3 (x=0) to pure Sb_2Te_3 (x=1)[8] with permission from Springer Nature.*

1.1.1 Topological Insulators' Physics and Applications

The unique properties of TIs lead to the emergence of novel physics and potential applications in quantum computing and spintronics. Breaking time-reversal symmetry (TRS), which is the symmetry of physical laws under time translation, in TIs is a great path for exploring their unique physics. Breaking TRS can be done by ferromagnetic ordering which can result from the magnetic doping of the TI or the interfacing with a magnetic layer[11,13]. This ordering leads to an energy gap at the Dirac point. Figure 1.2 illustrates such an effect. Breaking TRS has several quantum phenomena that have been experimentally demonstrated, including a topological magneto-electric effect, image magnetic monopole effect, topological Kerr and Faraday rotation, and the quantum anomalous Hall effect (QAHE)[11]. Another avenue to explore is topological crystalline insulators (TCI) symmetry breaking. The Dirac states in TCIs, unlike Tis, are not protected by TRS; instead, they are protected by structural crystalline symmetries[9]. This Symmetry breaking can be achieved by surface plasmon generation, charge transfer, and application of a periodic strain potential[14]. Breaking mirror symmetry on the surface leads to the acquisition of a variable mass in the Dirac nodes[9]. The mass variation is governed by the penetration depth of the surface states into the bulk. This could potentially be exploited in constructing a new generation of electronics. While TIs are more known for their spin-related properties, recent research has suggested that they could also exhibit valley polarization under certain conditions which can lead to valley-selective carrier

dynamics [15-17]. TIs are a promising candidate for various device applications. One of these device applications is the spin-filter. A spin-filter polarizes spins by using an external field[18]. Another device is the Chern Junction that can be used for operations like splitting, redirection, and switching of chiral edge currents in a topological circuit[19]. Figure 1.3 shows a Chern junction setup and different chiral edge currents.

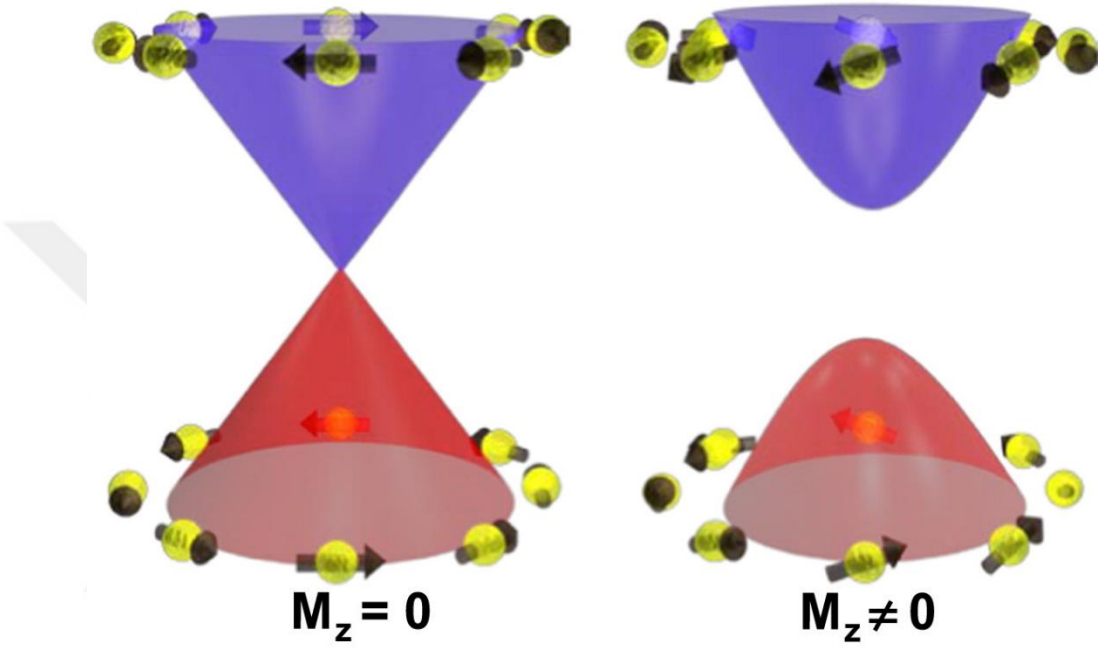

Figure 1.2: (a) The interplay among band topology, magnetic exchange, and structure engineering in the TRS-breaking phenomena. (b) Topological surface band diagram in undoped TI (massless) and magnetically doped TI (massive), respectively[13] with permission from Elsevier.

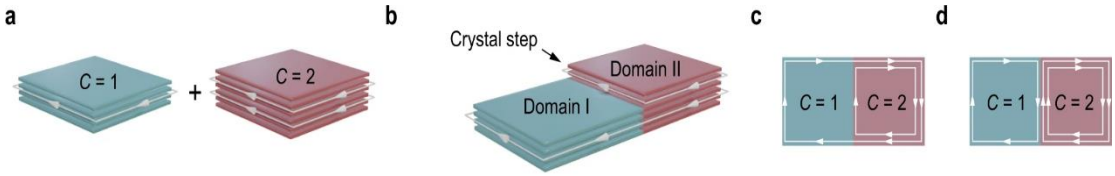

Figure 1.3: (a) A thinner MBT flake (Domain I) hosts a chiral edge state with Chern number C = 1 while a thicker flake (Domain II) hosts two chiral edge conduction channels with C = 2[19]. (b) A Chern junction is formed at a step in thickness in a single flake[19]. (c-d) Show two possible scenarios for the chiral edge states at the junction[19]with permission from Springer Nature.

Continuing with TIs potential applications, TIs can be explored for fault-tolerant quantum computation, they could redefine resistance standards, advance sensing applications, offer blueprints for novel magnetic memory, and they could be utilized for spin-based logic

devices, offering better specification compared to current electronics. When it comes to quantum computations, Majorana fermions are suggested to be the building blocks due to their non-Abelian statistics[23-25]. TI systems in proximity to superconductors can cause the appearance of Majorana fermions at the boundaries of the TI. For example, junctions of TIs such as Bismuth Selenide (Bi_2Se_3) nanowires that are coupled to conventional s-wave superconducting Tungsten (W) electrodes can realize robust superconductivity[26]. These Majorana states can be utilized as potential qubits with robustness against errors. For quantum resistance metrology, the QAHE in magnetic TIs such as Cr/V-doped (Bi, Sb)$_2Te_3$ allows access to the von Klitzing constant without an external magnetic field[27]. This offers a solution to the compatibility problem in quantum electrical standards. To demonstrate this, a multi-terminal TI device with circular Corbino geometry was used, showing that the effect can be stabilized for metrology applications[28]. For sensing applications, sensors based on Bi_2Te_3 nanostructures were fabricated and investigated[29,30]. These sensors exhibited noticeable changes in the conduction and polarization properties when exposed to different chemical environments[31]. This demonstrates that these properties can be reversibly tuned, highlighting Bi_2Te_3 as a potential multifunctional sensing material[31]. TI based magnetic memory can be achieved by the integration of TIs and magnetic tunnel junctions[32]. TIs exhibit high conversion efficiency due to the spin-momentum locking[32]. This property, accompanied with an ultralow switching current density, positions TIs as promising candidates for industry-level memory applications.

We have discussed the unique properties and possible device applications of TIs, but we have not mentioned arguably the most important phenomena of TIs, the QAHE. This phenomenon will be discussed in later in this chapter.

1.2 Previous Studies on Topological Insulators

Bi_2Te_3 is a crucial material in the study of TIs due to its narrow band gap, and robust surface states. The ease of synthesis of high-quality thin film from Bi_2Te_3 makes it ideal for theoretical studies and practical applications. This subchapter this in detail, highlighting Bi_2Te_3's role in advancing the field of TIs.

1.2.1 Bi_2Te_3 Merits

Ultimately, practical applications drive any type of research, and for that purpose, narrowing down the candidate chemistries for TIs is quite important. Regardless of their unique properties, TIs are not all practically viable. Several factors influence the right choice of the TI chemistry. These factors include the band gap size, the quality of surface states, stability, ease of doping, and scalability[33]. These factors aim to prevent current leakage, inefficient switching, maximize mobility, minimize scattering, allow fine tuning of electrical properties, and to offer scalability for mass production at low cost[33]. In this regard, Bi_2Te_3 and its doped variants are favored. Bi_2Te_3 offers a desirable large bulk band gap, and has well-characterized and robust surface states[5,33]. Additionally, Bi_2Te_3 can be easily doped with elements like Sb or Selenium (Se)[33]. Moreover, it is commercially available and extensively studied making it a convenient choice for experimentation and prototyping. Furthermore, Bi_2Te_3-based thin films and nanostructures fabrication is in line with semiconductor industry standards. To add more, Bi_2Te_3 and its doped variants have high thermoelectric figure of merit (ZT) among thermoelectric materials, their unique properties from the band structures and the topologically protected surface states to the spin-momentum locking mechanism make them a crucial chemistry to focus on when it comes to TIs[34-36]. Bi_2Te_3 exhibits the Seebeck effect where the voltage across the material is influenced by the temperature gradient and the opposite Peltier effect[37]. The distinct rhombohedral lattice and weak van der Waals bonding crystal structure of Bi_2X_3 (where X = Se, Te, Sb) materials, provides them with an anisotropic character like other Two-Dimensional (2D)-layered materials, leading to unique electronic and transport properties[5].

1.2.2 Bi_2Te_3 and its characteristics

Achieving the properties discussed earlier requires high-quality thin films which can be achieved with epitaxial growth. This process ensures the coherency of the thin film and the substrate, reduces defect densities, promotes smooth surface morphologies, and minimizes interfacial resistance. These high-quality thin films exhibit improved electrical and thermal transport properties.

Bi_2Te_3 growth involves many different techniques and many steps. In here we will describe a typical molecular beam epitaxy (MBE) process. It all starts with substrate

preparation which differs depending on the type of substrate being used. The substrate is then loaded into the ultra-high vacuum (UHV) chamber and annealed for a certain amount of time depending on its type. The deposition starts after the annealing process where careful control of Bi and Te flux is important. The Duration of the deposition in addition to the Bi and Te cell temperature and the substrate temperature directly affect the quality and the thickness of the thin film. The substrate is annealed after deposition to further improve the surface quality. In the following we will review some of the reported growth of Bi_2Te_3 and its doped variants on different substrates and some of the characterization results.

In ref. 6, films were grown on silicon (Si) (111). The layer-by-layer growth involved a highly Te-rich environment with specific temperature conditions ($T_{Bi} > T_{Si} \geq T_{Te}$). Reflection high-energy electron diffraction (RHEED) was used to monitor growth dynamics, with each RHEED intensity oscillation corresponding to the deposition of one quintuple layer (QL) of Bi_2Te_3. Angle-resolved photoemission spectroscopy (ARPES) was used to study the electronic band structure, confirming the presence of massless Dirac-like surface states[6]. Scanning tunneling microscopy (STM) images showed standing waves of the surface states, indicating their topological property[6]. Voltage-dependent standing wave patterns were used to determine the energy dispersion, confirming the Dirac cone structure[6]. Backscattering of topological states by nonmagnetic impurities was reported to be completely suppressed, confirming the TRS and the topological nature of the surface states[6].

In ref. 12, The growth of Bi_2Te_3 was also done by MBE on Si (111). Initially, the Si substrates were chemically cleaning using the HF-last RCA procedure to eliminate prior oxidation and passivate the surface with hydrogen[12]. Subsequently, the substrates were heated in situ to 600 °C for 20 minutes to desorb the hydrogen atoms from the surface[12]. The growth process occurred under UHV conditions with a base pressure of around 1×10^{-9} mbar. During growth, the pressure was maintained below 5×10^{-8} mbar[12]. Techniques such as X-ray diffraction (XRD), X-ray reflectivity (XRR), atomic force microscopy (AFM), and ARPES were employed for characterization. The crystal structure, layer thickness, and quality of the films were determined by XRD and XRR. AFM showed smooth terraces and plateaus, which are essential for certain applications.

ARPES and AFM results are shown in Figure 1.4 reveal the Dirac states and the band inversion.

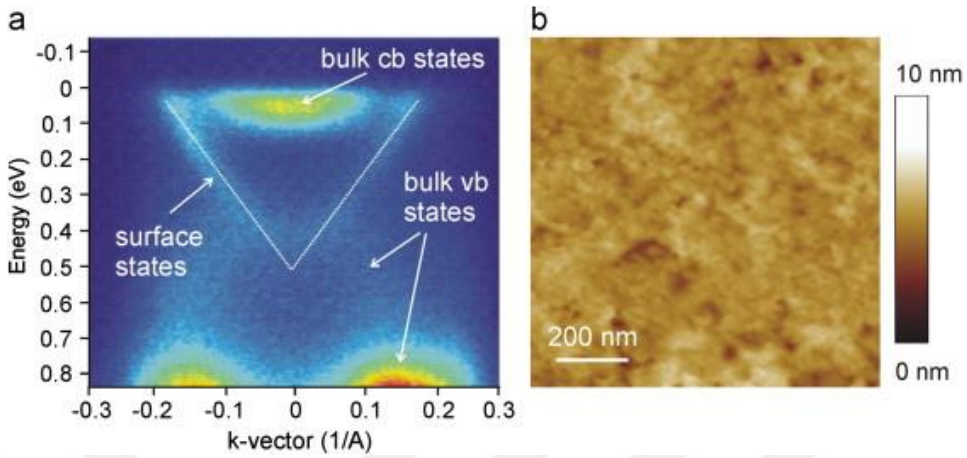

Figure 1.4: (a) ARPES spectrum from a sputtered and annealed Bi_2Te_3 layer taken along the $\bar{\Gamma}\bar{K}$ direction[12]. (b) AFM image of a sputtered and annealed Bi_2Te_3 sample[12] with permission from Elsevier.

In ref. 38, Bi_2Te_3 thin films were deposited on a clean Sapphire (Al_2O_3) (0001) substrate that was place in an Excel Instruments sputtering system. The chamber was evacuated to a base pressure of approximately 1 x 10^{-7} Torr[38]. Two separate targets of high-purity (99.99%) Bi and Te, each 2" in diameter, were used for the co-sputtering process. The substrate was heated to a temperature of 573 K (300 °C)[38]. During deposition, Argon gas was introduced into the chamber at a flow rate of 12 standard cubic centimeter per minute (sccm) increasing the pressure to 8.4 x 10^{-4}. DC power was applied to the Bi and Te targets at fixed values of 5 W and 9 W[38]. The resistivity measurements reveal distinct behaviors at low and high temperatures, indicating different electron-phonon scattering mechanisms[38]. The analysis suggested that electron-phonon scattering due to defects and disorder is less dominant, with 2D electron-electron interaction effects playing a crucial role at low temperatures. In contrast, at high temperatures, electron-phonon interaction dominated[38]. Hall effect measurements indicated n-type behavior in the film, with a sheet carrier density of the order of 10^{12} cm^{-2}. The mobility was estimated to be around 50 cm^2 V^{-1} s^{-1}, slightly decreasing with increasing temperature due to enhanced electron-phonon scattering. The analysis highlighted the contribution of both surface and bulk channels to electron transport in these Bi_2Te_3 films. The temperature dependence of the sheet resistivity of the Bi_2Te_3 film is shown in Figure 1.5a and Hall resistivity with the magnetic field recorded at different temperatures in Figure 1.5b.

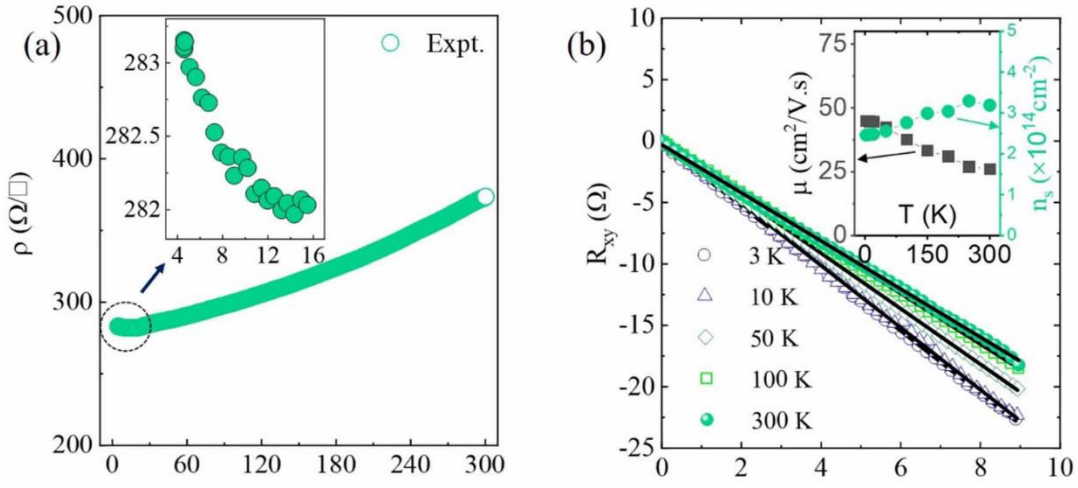

Figure 1.5: (a) Sheet resistivity as a function of T (4–300 K) of the Bi_2Te_3 film. Inset shows the data at low T (4–15 K) (b) Hall resistivity with the magnetic field recorded at different T[38]. Sheet carrier concentration (solid circle symbols) and mobility (solid square symbols) at different T are shown in the inset[38] with permission from IOP Publishing.

In 39, Bi_2Te_3 thin films were grown on Al_2O_3 (001) substrates using Pulsed Laser Deposition (PLD) with a Bi_2Te_8 target[39]. This target was used to solve issues with high doping carriers and to avoid Te-deficient phases[39]. The PLD process was carried out at 3.7 J/cm^2 lase fluence and a repetition rate of 1 Hz, while the pressure in the growth chamber was maintained below 2×10^{-6} Torr[39]. Substrates were cleaned using ultrasonication in acetone, methanol, and deionized water prior to deposition[39]. Helium gas was introduced throughout the deposition process, with the pressure maintained at 210 mTorr. The optimal substrate temperature for the growth process was determined to be 225°C, and the film thickness was controlled by varying the number of laser pulses from 200 to 1500, resulting in thicknesses ranging from 16 to 152 nm[39]. XRD patterns confirmed the films' preferred orientation along the (003) direction. Raman spectroscopy showed characteristic phonon modes at 102.5 cm^{-1} and 134.8 cm^{-1}. AFM images illustrated smooth and uniform surface morphologies, with an increase in surface roughness from 1.2 nm to 3.4 nm as the film thickness increases. Electrical measurements demonstrated a decrease in resistivity with increasing film thickness, due to the increase in carrier concentration from 2.0×10^{19} cm^{-3} to 4.4×10^{19} cm^{-3}, while the carrier mobility showed a slight increase and subsequent decrease[39]. Temperature-dependent resistivity measurements indicate metallic behavior at room temperature, transitioning to electron-electron interaction at lower temperatures due to disorder. Magnetoresistance measurements revealed that thinner films exhibited a single phase-coherent channel, and

thicker films displayed two decoupled conduction channels[39]. These results suggest that the transport properties of Bi_2Te_3 films are influenced by their thickness. Figure 1.6 shows the magnetoresistance measurements of different thickness films.

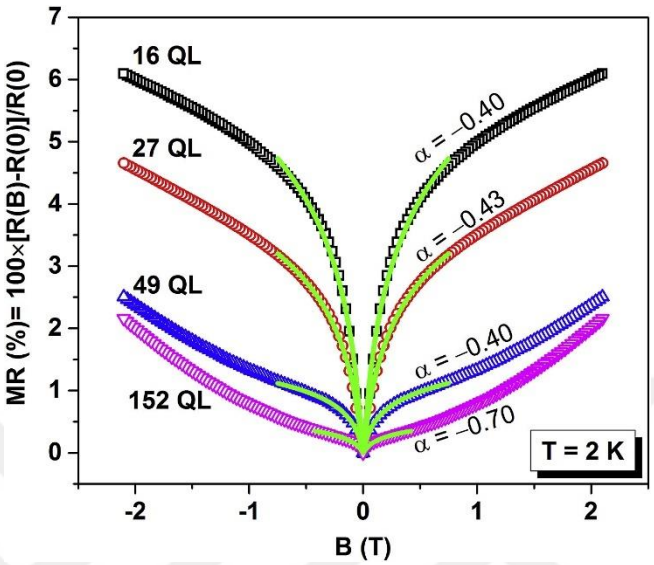

Figure 1.6: Magnetoresistance [MR (%), B = ± 2.1 T] of Bi_2Te_3 films with various thicknesses at 2 K. The solid green lines in low B are the theoretical predictions of 2D weak antilocalization (WAL)[39] with permission from Elsevier.

1.2.3 Doped Bi_2Te_3 and Its Characteristics

In ref. 8, $(Bi_{1-x}Sb_x)_2Te_3$ films were deposited on Al_2O_3 using MBE. The MBE-ARPES-STM combined system used for this study operates at a base pressure of 1×10^{-10} Torr. Prior to film growth, the Al_2O_3 substrates were degassed at 650 °C for 90 minutes followed by 850 °C for 30 minutes[8]. High-purity Bi (99.9999%), Sb (99.9999%), and Te (99.999%) were evaporated from Knudsen cells[8]. Te-rich conditions were maintained to minimize vacancies, with the substrate temperature at 180 °C[8]. ARPES measurements showed Dirac-like topological surface states across the entire composition range ($0\leq x\leq1$), with varying Dirac cone geometry as a function of x. The increase in Sb lead to a steeper slope of the Dirac line, which indicated higher fermion velocity, while the E_F shifted downward from the bulk conduction band (BCB). At x=0.88, both the DP and EF lie within the bulk energy gap.[8]. Furthermore, the transition from electron- to hole-type occurred between x=0.94 and 0.96[8]. The robust presence of topological surface states across the entire composition range highlighted the stability of the nontrivial Z_2 topology against alloying[8]. Transport measurements revealed that resistivity increases, and

insulating behavior strengthens with higher Sb content[8,40]. These results showed the evolution of the Dirac band properties and their impact on the transport behavior in,

In ref. 41, Cobalt (Co)-doped Bi_2Te_3 was deposited using DC magnetron sputtering on Si (111) substrates. The base pressure was 5×10^{-8} Torr and the working pressure was 3 mTorr[41]. The doping concentrations of Co ranged from 0.04 to 0.4. The deposition rates were 1 nm/s for Bi_2Te_3 and 0.1 nm/s for Co and substrate temperature was 300 °C during deposition which minimized defect formation in the films[41]. XRD revealed the successful incorporation of Co into the Bi_2Te_3 lattice[41]. Magneto-transport measurements revealed a transition from metallic to semiconducting behavior[41]. The undoped Bi_2Te_3 film exhibited metallic behavior, with the E_F assumed to be within the band gap[41]. Co doping led to the destruction of surface states, causing the E_F to shift between the conduction and valence bands. The magnetoresistance of the films displayed a non-saturating positive behavior with increasing magnetic field, indicating the presence of WAL effects. This was further supported by the observation of a logarithmic variation in magnetoconductivity at low magnetic fields, a characteristic feature of materials with strong spin-orbit coupling. Overall, the systematic growth and comprehensive magneto-transport characterization of Co-doped Bi_2Te_3 films offer valuable insights into the behavior of topological insulators in the presence of magnetic dopants. Figure 1.7 shows the undoped and doped magneto resistance of Bi_2Te_3 Films[41].

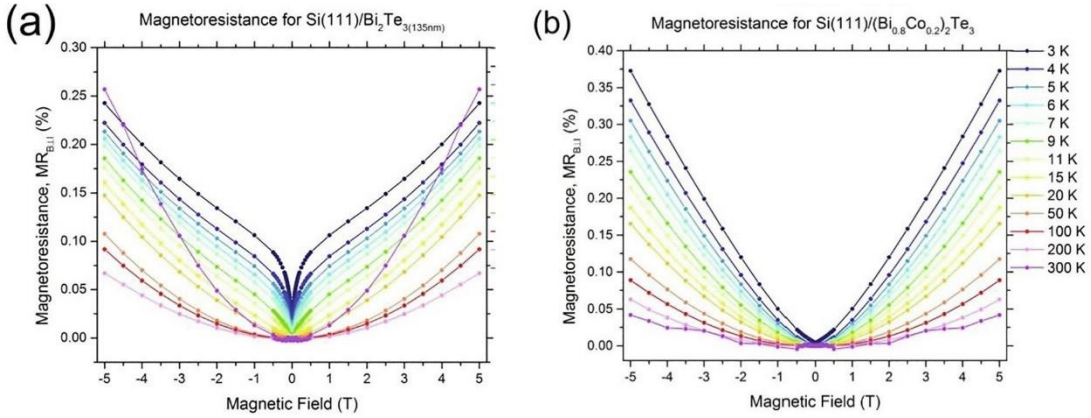

Figure 1.7: (a) Magnetoresistance of pure Bi_2Te_3 films[41]. (b) Magnetoresistance curves of Co-doped $(Bi_{1-x}Co_x)_2Te_3$ films with x = 0.2[41] with permission from Elsevier.

1.2.4 The Quantum Anomalous Hall Effect

The QAHE is defined as the quantization of the Hall conductance in the absence of an external magnetic field. This effect was theoretically predicted by Duncan Haldane in 1988 in a model of electrons on a honeycomb lattice with non-zero Chern numbers[20,42]. The QAHE was experimentally achieved in 2013 with Cr-doped (Bi, Sb)$_2$Te$_3$ films, followed by V-doped (Bi, Sb)$_2$Te$_3$ films in 2015 [20,22]. These theoretical and experimental results demonstrated the crucial role of magnetic doping and non-trivial states for the QAHE. Magnetic doping has its limitations, such as sample quality degradation and a decrease in the critical temperature of the QAH state.

The work to go beyond these limitations led the discovery of the QAHE in MnBi$_2$Te$_4$ flakes[21]. Additionally, the QAHE has been observed in moiré superlattice systems, including twisted bilayer graphene (TBG)[43,44], ABC tri-layer graphene on hexagonal boron nitride (h-BN)[45], and transition metal dichalcogenide (TMD) heterostructures[45]. The immense potential that the QAHE holds when it comes to applications in quantum information devices, spintronics and other technologies makes pursuing it even more exciting.

The QAHE has been studied in thin films of $Cr_{0.15}(Bi_{0.1}Sb_{0.9})_{1.85}Te_3$ grown on $SrTiO_3$ substrates[22]. These films allow the transition of carrier type between n-type and p-type by using gate voltage. The Hall resistance measurements of these films show a linear dependency of the magnetic field on the temperature at high values due to the Hall effect. On the other hand, the anomalous Hall effect characteristic hysteresis loop shows at low temperatures[22]. This is also an indication of ferromagnetic order in the thin film[22]. The observation of a distinct plateau in the zero field Hall resistance, quantized to h/e2, confirms the discovery of the QAHE in these films.

Further research showed that the QAH state is robust and can be manipulated by a gate voltage, with the Hall resistance remaining quantized even at high magnetic fields[22]. The enhanced MR in the QAH state indicates a difference in transport properties between an ordinary insulator and a QAH insulator[22]. The temperature dependence behavior of the QAH state is like that of integer quantum Hall systems which suggests variable range hopping mechanisms.

Comparing with the work investigating the QAHE in V-doped (Bi, Sb)$_2$Te$_3$, we see that the V-doped films show a higher curry temperature and coercive field but lower 2D carrier density[20]. This shows that the V-doped films could be much more reliable for the QAHE and its applications[20]. The lower 2D carrier density makes it so less doping is required to make the system charge neutral[20]. The realization of the QAH effect in these magnetic TIs opens possibilities for developing low-power-consumption, topological quantum electronic and spintronic devices without the need for an external magnetic field.

The growth process and its kinetics for epitaxial Bi_2Te_3 and its doped variants have not been completely understood. Precisely controlled growth conditions (under different effusion cells and substrate temperatures, flux rates, heating rates) and kinetics must be further studied for the new physics and the devices of TI's.

1.3 Thesis Aims

In this thesis, we aim to identify the growth conditions needed for optimized thin film TI materials, specifically Bi_2Te_3 and Sb-doped Bi_2Te_3. We discuss the growth conditions and the kinetics that lead to different growth modes. We focus on deposition, adsorption, desorption, and surface diffusion phenomena. We investigate our characterization data to showcase the effect of the growth optimization on the quality and properties of the thin films that we deposited. Through these investigations, this thesis seeks to contribute to the advancement of understanding in this field and potentially pave the way for enhanced control and utilization of TI materials in future applications.

1.4 Contribution of This Thesis

The research presented in this thesis has been submitted to several conferences, including the European Materials Research Society (E-MRS), NanoTR, and the International Conference on Quantum Materials and Technologies (ICQM). It has been presented at ICQM 2024 and NanoTR 2024. Moving forward, this work will be expanded and refined with additional data and analyses, which will be detailed in a later chapter. Our experimental results are being prepared for publication, ensuring that the final manuscript reflects the most comprehensive and up-to-date findings.

Chapter 2:
METHODS

The phenomena exhibited by specifically magnetic TIs and generally magnetic thin films are critical for the future of spintronics and magnetic storage technologies. These thin films are created using sophisticate methods like sputtering, MBE, and PLD. The deposition techniques mentioned allow for a uniform, and high-quality thin films with precise control over the stoichiometry. This is achieved using UHV environments that minimizes contamination. Additionally, these methods provide a wide range of substrate temperature from room temperature to above 800 ℃, allowing for the customization of film properties. Moreover, techniques like RHEED provide in situ monitoring and characterization, enabling real-time adjustments to optimize film quality. Overall, these deposition techniques are essential for developing advanced thin films with tailored properties for various applications.

2.1 Deposition Methods

The deposition process depends on multiple factors such as temperature, pressure, diffusion constant, the pressure of forming gas, and stoichiometry. There are 3 deposition modes for thin films: island growth (Volmer -Weber), layer-by-layer growth (Frank–Van der Merwe), and Stranski–Krastanov growth[46]. Island growth is when the deposited material forms 3D islands on the substrate[46]. This is typically observed when metals and semiconductors are deposited on oxide substrates. Layer-by-layer growth is when the deposited atoms or molecules spread uniformly across the substrate forming sheets[46]. This occurs due to the stronger binding of the deposited material to the substrate than to itself. Finally, the Stranski–Krastanov growth is a combination of the previously mentioned modes where the deposition starts as a layer-by-layer and then 3D islands start forming on the initial layers[46]. Figure one is an illustration of the discussed deposition modes.

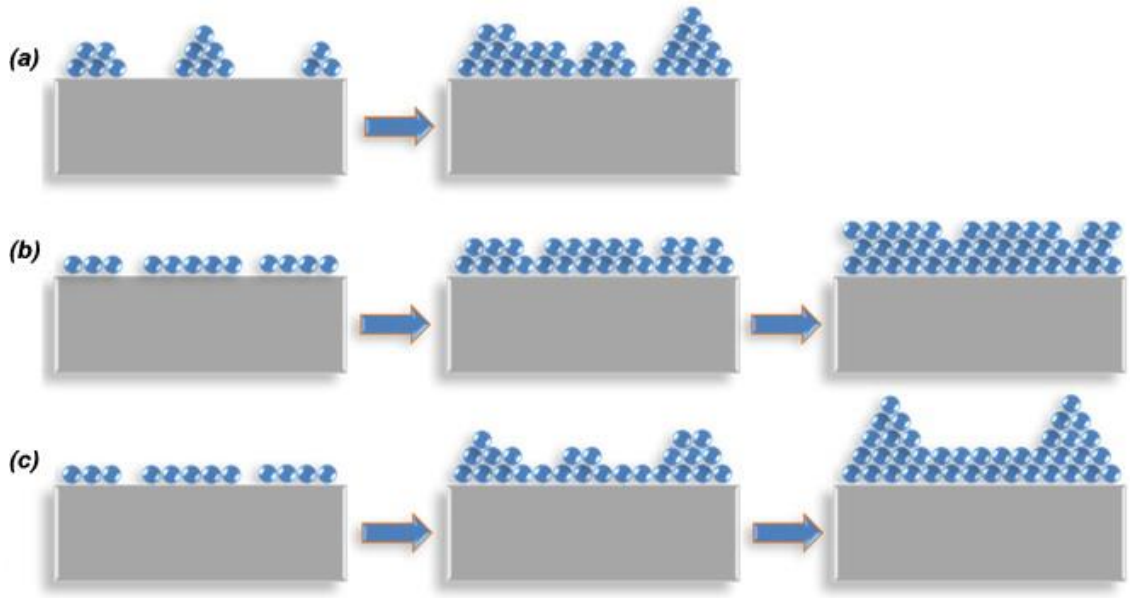

Figure 2.1: Illustrations of the basic growth modes including (a) Volmer–Weber (island), (b) Frank–Van der Merwe (layer-by-layer), and (c) Stranski–Krastanov growth[46] with permission from Elsevier.

2.1.1 Epitaxial Growth

Epitaxial growth is a process which crystalline material grows on a substrate where the atoms of the deposited material follow the crystal arrangement of the substrate. This results in the inheritance of the crystallographic orientation and lattice structure of the substrate by the deposited material. There are two main types of epitaxial growth: Heteroepitaxy and Homoepitaxy. Heteroepitaxy occurs when the material being deposited, and the substrate material are different but have similar crystal structures[47]. The second type, Homoepitaxy, is when the deposited material is the same as the substrate[47]. Our research mainly focuses on Heteroepitaxy. A small lattice mismatch between two crystals is important for epitaxial growth to minimizes the interfacial energy [48].

2.1.2 PLD

PLD is one of the most important deposition techniques that used to deposit a wide range of materials on a wide range of substrates and offers precise and wide tunability of the deposition parameters. It is a great method for the fabrication of high-quality films for various electronic, magnetic, and optical applications [49-53]. PLD is based on the interaction between the high-energy pulsed laser and the target material to be deposited[49-53]. This

energetic interaction generates a plume of atoms that get deposited on a substrate [49-53]. The pulsed laser beam is directed onto the surface of the target material that sits a rotating holder in a carrousel. The process takes place in UHV. The laser is usually an ultraviolet excimer laser, such as KrF[51]. The laser causes the target to rapidly heat up and ablate which creates a plume of high energy deposition material[49-53]. Depending on the setup, the laser is guided with an optical setup towards the target. The target's optical, topological, and thermodynamic properties dictate the energy and frequency of the pulsed laser needed to create a plume. The plume is highly forward directed, and it expands away from the target creating a deposition zone[49-53]. The substrate sits in height adjustable stage and is positioned in the deposition zone. The plume interacts with the surface of the substrate and adheres to it, forming a crystalline thin film[49-53]. The laser beam is scanned across the rotating target to provide a larger deposition zone [4-8]. Figure 2.2 shows an illustration of the PLD process and an inset image of the plume on the top, and Figure 2.3 shows our own PLD setup.

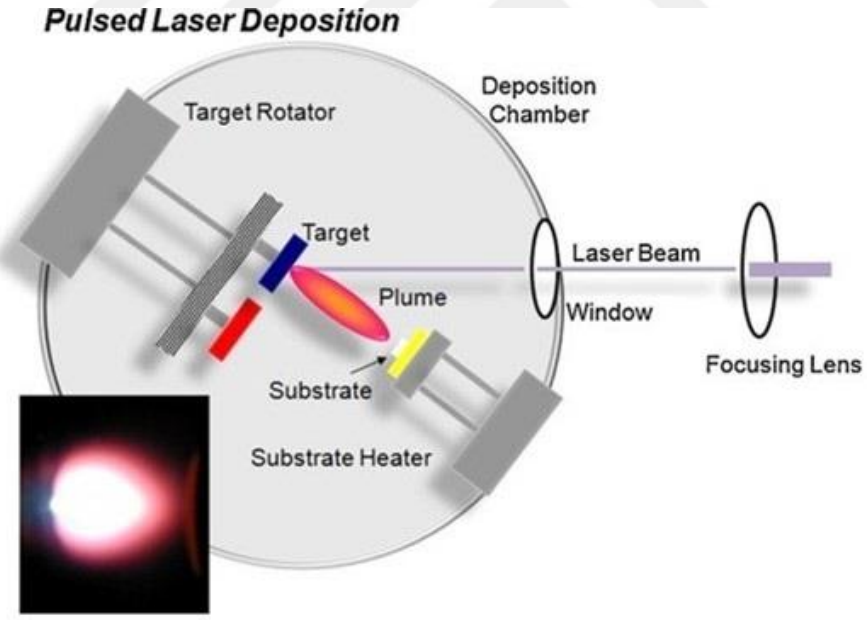

Figure 2.2: Schematic of a standard pulsed laser deposition system. The inset picture shows an actual photograph of the plume[46] with permission from Elsevier.

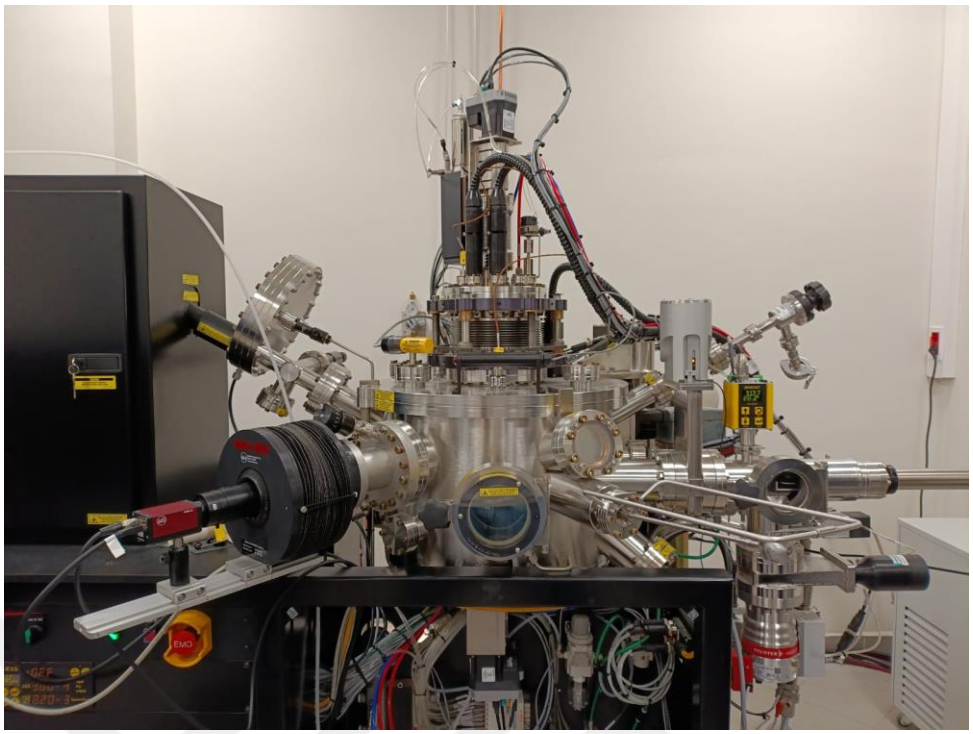

Figure 2.3: PLD setup in our lab.

The deposition is carried out in a reactive environment due to the introduction of a partial pressure of a background gas like oxygen. This increases the working pressure from the base pressure by 3 to 4 orders of magnitude based on my experience in the laboratory and the recipes, that depend on the material being deposited amongst other factors. The background gas is controlled using a mass flow controller. The background gas interacts with the ablated material to enhance phase formation, achieving desired stoichiometry, and reduction of the kinetic energies of the ablated material. The temperature of the substrate can also be controlled using the substrate heater. The deposition rate depends on factors such as laser spot size, pulse rate, pulse energy, target to substrate distance, background gas partial pressure, and the chamber's base pressure.

PLD provides many advantages including:

- Deposition of wide range of materials including oxides, semiconductors, metals, and complex compounds especially because the laser source is outside the vacuum chamber.
- PLD can maintain the stoichiometry of the target material in the thin film.
- Ablated species have kinetic energies that support surface mobility.

- PLD provides real-time monitoring and control of film deposition using in-situ characterization methods like RHEED.

2.1.3 MBE

MBE is another widely used deposition technique. It is used in research and the fabrication of many devices like transistors, topological insulators, super conductors, and other structures for quantum computing applications and others[49,50,54-56]. MBE operate under UHV conditions to minimize contamination and interference[49,50,54-56]. The MBE system contains multiple effusion cells where each can have a different source material. When the source material is heated, it evaporates and forms a beam of atoms or molecules that travels in a collimated beam towards the substrate[49,50,54-56]. The substrate sits in a rotatable, temperature and height-adjustable growth stage[49,50,54-56]. Each effusion cell is controlled independently allowing for precise control over the deposition rates. The incoming atoms or molecules condense on the substrate surface and form a single atomic or molecular layer. This process is repeated until the desired film thickness and composition is achieved. The growth stage has its own heater allowing the deposition of materials at different substrate temperatures. This allows us to study thin films at different growth kinetics. The deposition rate and thickness of deposited material is monitored using in-situ crystal monitors. In addition, the MBE provides in-situ RHEED characterization to observe the crystallographic and surface quality of the growing film in real time. Our MBE system also has electron beam gun deposition. The material needed is placed in the available crucible position on the e-beam source tray. The material is then targeted by a high-energy electron beam, generated by an electron gun. The energy from the focused beam is absorbed by the material. Rapidly heating it and evaporating it. The evaporation creates a plume of vaporized material that is then deposited on the substrate. Figure 2.4 shows an illustration of the MBE process.

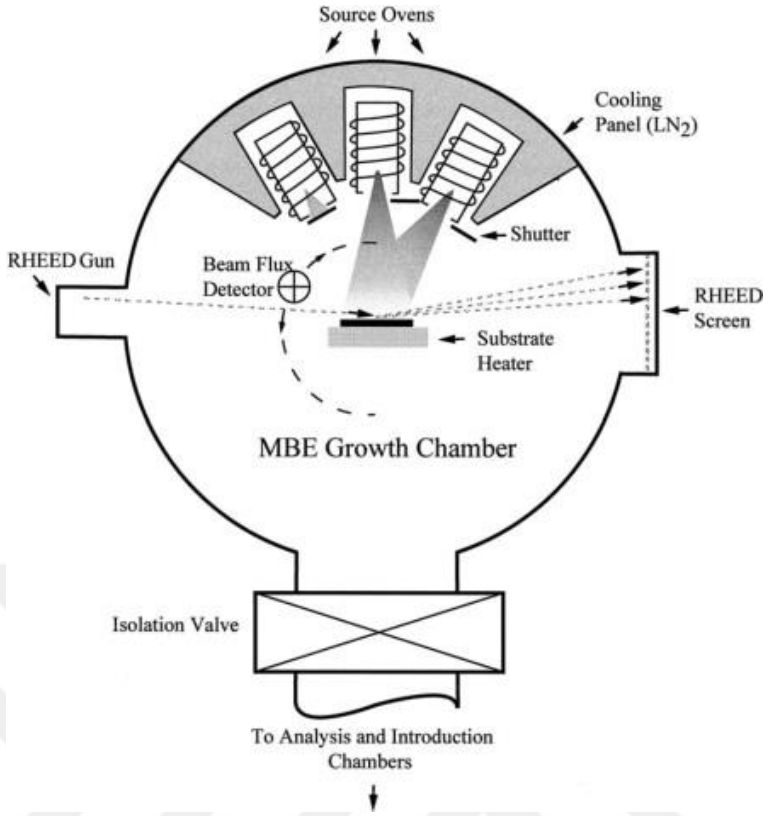

Figure 2.4: Top view of a simple MBE chamber showing the essential growth sources, shutters, beam flux detector and the RHEED system for monitoring structure during growth[57] with permission from Elsevier.

The MBE system provides many advantages including:

- Exceptional control over the composition of the layers due to the independently controlled effusion cells, enabling the growth of multi-component materials.
- MBE can operate at low substrate temperatures.
- Wide range of materials can be deposited.

2.1.4 Sputtering

Sputtering is another great method that is used to deposit a wide range of functional materials with very different compositions such as magnetic insulators, dielectrics, and magneto-resistive superconducting oxide materials[49,50,54,58-61]. Sputtering offers precise control over the stoichiometry and structure. It supports scalable production. The way sputtering works is by the removing of atoms or molecules from a solid target material through the bombardment of energetic ions[49,50,54,58-61]. The process takes place in UHV to

minimize contamination and create a controlled environment. A high-purity inert gas, such as Argon, is introduced into the chamber at a certain pressure and then high-voltage electrical field is applied between the target and the substrate to create ionized particles,[50,54,58-61]. These ions are accelerated towards the target due to the electrical field[49,50,54,58-61]. The accelerated ions collide with the target which leads to the ejection of target atoms or molecules. The ejected particles referred to as sputtered particles are then free to move towards the substrate. The target acts as the cathode and the substrate acts as the anode in the sputtering setup. The sputtered particles travel the substrate forming a thin film. the power source can either be a direct current or an alternating current (RF). The properties of the thin film are influenced by many parameters including gas pressure, target material, target to substrate distance, power applied and substrate temperature. Figure 2.5 shows an illustration of sputtering on the left, and magnetron sputtering on the right.

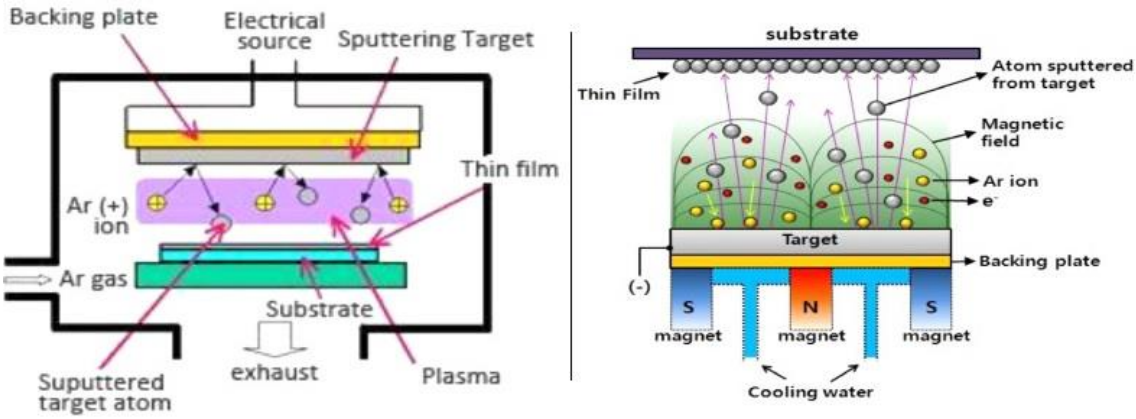

Figure 2.5: Sputtered deposition technique on the left, and Magnetron sputtering deposition on the right[50] with permission from Elsevier.

The sputtering chamber available in our lab is shown in Figure 2.6.

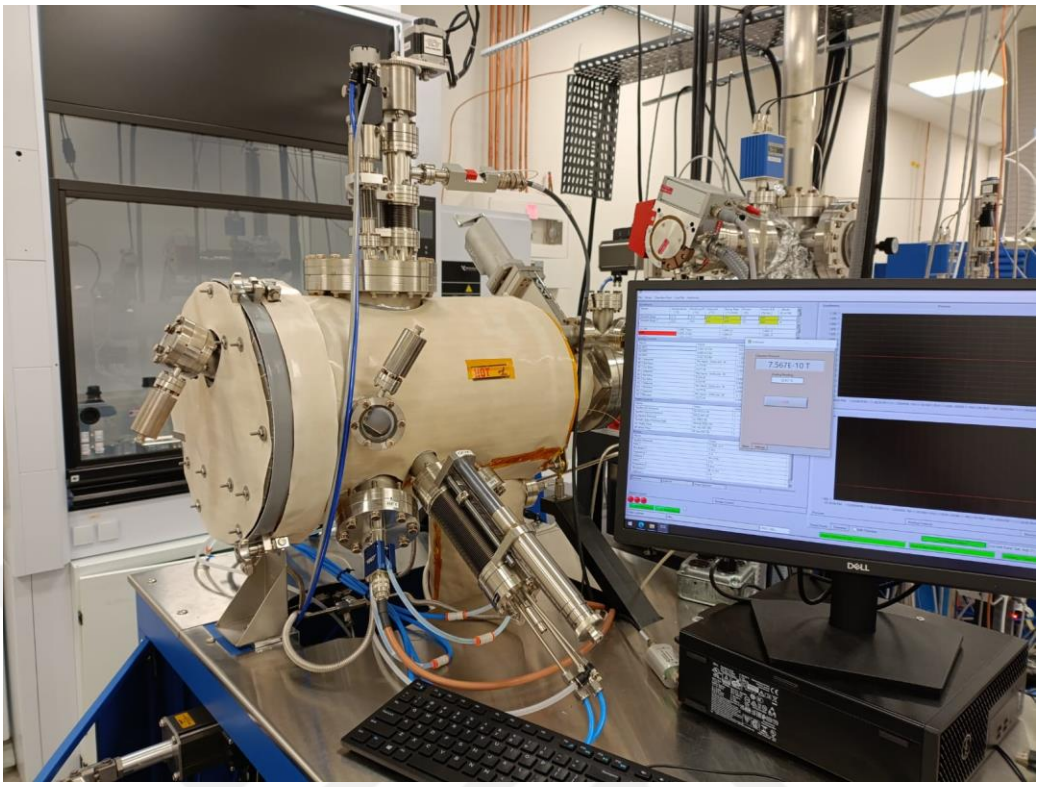

Figure 2.6: Sputtering chamber in our lab.

Sputtering provides many advantages including:

- Sputtering can deposit a wide range of materials with precise control over film composition and thickness.
- The process produces films with excellent uniformity, purity, and adhesion, even on complex geometries and sensitive substrates.
- Sputtering is scalable for industrial applications and produces films with superior properties like increased hardness and improved electrical conductivity, suitable for various substrates.

2.2 Characterization

2.2.1 XRD

XRD is a powerful technique used to investigate the structural properties of crystalline materials[62-65]. XRD offers a way to study the interactions of the incident X-rays with the material's crystal lattice[62-65]. When X-rays interact with the material's atoms, they scatter

in different directions[62-65]. This scattering is not random and depends on the arrangement of atoms in the crystal[62-65]. Bragg's law is the principle behind the XRD. It relates the angle of the incident X-rays, the wavelength of the X-rays, and the spacing between the planes of atoms in the crystal lattice[62-65]. Bragg's Law is expressed as $n\lambda=2d\sin\theta$, where n is the order of diffraction, λ is the wavelength of the incident X-rays, d is the distance between the planes in the crystal, and θ is the angle of incidence. Constructive interference occurs when the difference of the path length between scattered X-rays is equal to an integer multiple of the X-ray's wavelength[62-65]. This creates distinct peaks in the diffraction pattern. These distinct peaks provide great information on the crystal. XRD has numerous applications in materials science, chemistry, geology, physics, and engineering. It is primarily used to determine the crystal structure of materials. We can extract information on the unit cell, form its size to its symmetry[62-65]. For instance, XRD can identify unknown materials by comparing their diffraction patterns to reference databases of known compounds. This makes it a vital tool in fields such as mineralogy. Moreover, XRD can identify different phases in a multiphase material[62-65]. This is crucial because the performance of a material may depend on the presence different phases and their ratios. Additionally, XRD can be used to study crystallite size and strain in the material. The broadening of diffraction peaks can provide information about the average size of crystallites and internal stresses or defects. The smaller the crystallite, the broader the peaks. The versatility and non-destructive nature of XRD make it an indispensable tool in both research and industry. It can analyze samples in various forms. XRD remains a cornerstone technique for understanding the structural properties of materials and continues to evolve with advances in instrumentation and data analysis methodologies. Figure 2.7 shows an illustration of Braggs' equation and figure 2.8 shows an illustration of the components of the X-ray diffractometer.

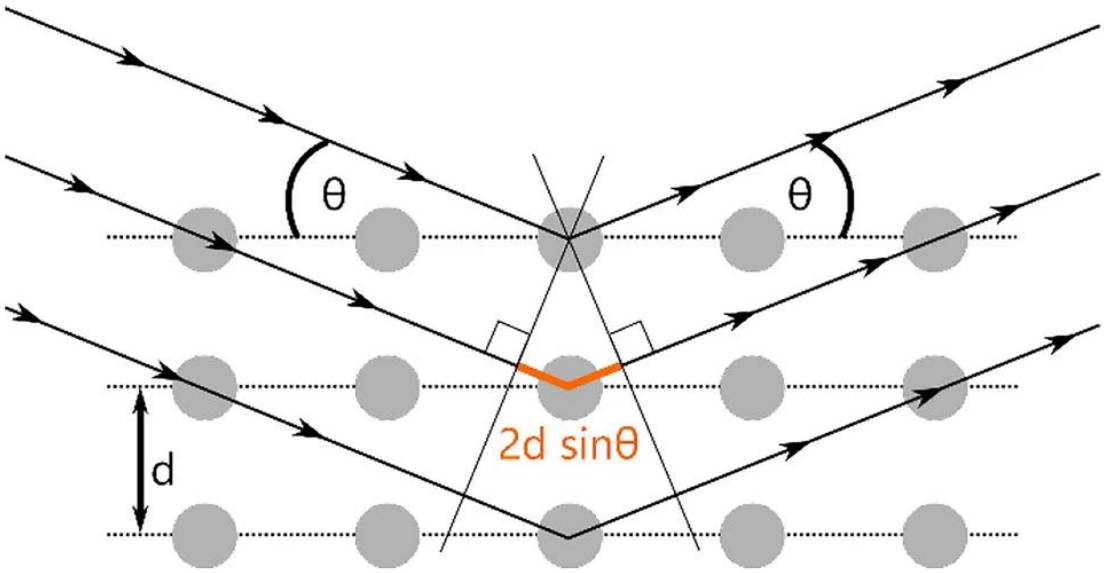

Figure 2.7: Visualization of Braggs' Equation[64] with permission from Springer Nature.

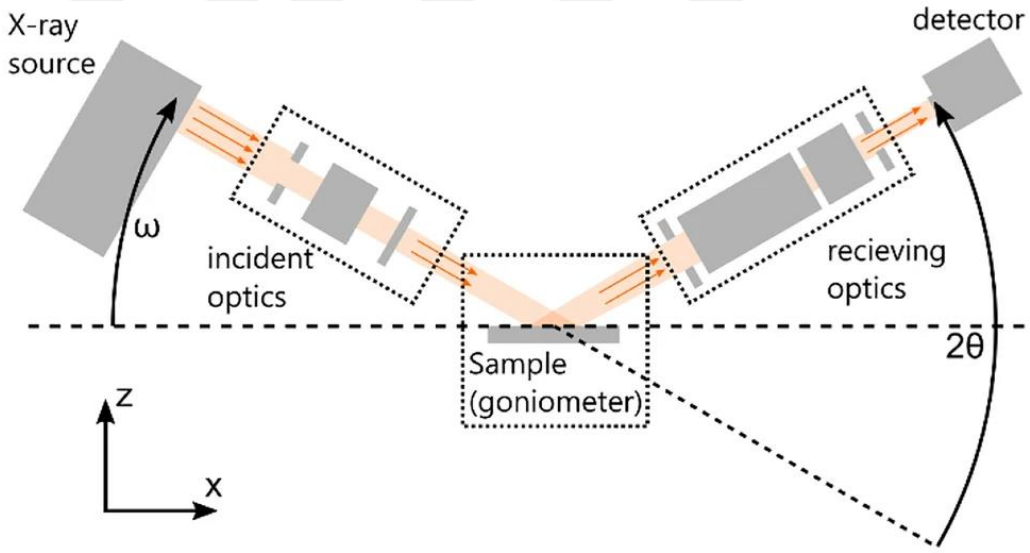

Figure 2.8: Components of a diffractometer[64] with permission from Springer Nature.

Table 2.1 shows the typical peaks in an XRD pattern of a successfully grown Bi_2Te_3 thin film and their corresponding miller indices.

Table 2.1: relevant peak positions and corresponding miller indices of Bi_2Te_3 (ICSD reference code: 96-901-1963)

Position(2θ)	17.3	27.6	44.8
Miller Indices	(003)	(006)	(0015)

2.2.2 XRR

XRR is a technique that provides complementary information to techniques like XRD. XRR works at shallow angles, and it measures the intensity of the reflected X-rays from the material's surface with respect to the incident angles[62-66]. The resulting reflectivity pattern, characterized by a series of oscillations known as Kiessig fringes, reveals details about the sample's properties[62-66]. The period of these fringes is directly related to the thickness of the film layers, allowing for highly accurate measurements of layer thickness. Additionally, the properties of the fringes in the reflection pattern from the amplitude to the spacing offer information on the density of the layers, as well as the quality of interfaces between different materials in the film. Moreover, the roughness of the thin film can be studied by analyzing the rate of decay of the reflected intensity. It's important to note that the reflected intensity decreases with increasing angle. Smoother surfaces show slower decay while rougher surfaces show a faster decay. This provides valuable information for the optimization of the synthesis process of the thin films. XRR is valuable in many fields, including microelectronics, optics, and materials science. XRR is a non-destructive technique and is sensitive to electron density variation making it ideal for studying a wide variety of materials.

2.2.3 AFM

AFM is a great technique for high-resolution analysis of the surfaces of thin film. It analyzes the topography and gives us information on the surface roughness. In AFM the surface of the material is scanned with a sharp tip of nanometer dimensions[62 63,67]. This tip is connected to a flexible cantilever[62,63,67]. The cantilever deflects in response to the force of the interaction between the tip and the material[62,63,67]. AFM can operate in several modes, with the two primary ones being contact and non-contact modes. In contact mode, the tip physically touches the surface, which can provide high-resolution data but may damage some samples[62,63,67]. In contrast, non-contact mode is preferred because the tip hovers above the surface without any physical contact which avoids and minimizes the risk of sample damage while still gathering accurate information[62,63,67]. A laser is directed at the back of the cantilever and is reflected onto a photodetector[62,63,67]. The deflections change the position of the reflected laser beam on the photodetector, allowing for precise

measurement of the surface's features. Figure 2.9 illustrates an AFM setup in non-contact mode.

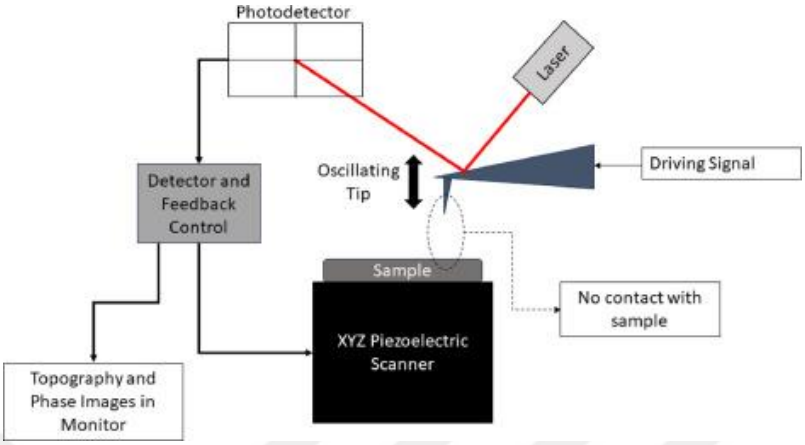

Figure 2.9: Working mode of non-contact mode[67] with permission from Elsevier.

2.2.4 RHEED

RHEED is a great in-situ technique that give important information on the surface structure of the material. RHEED is used to see the evolution of the deposition process by providing information on the initial surface structure of the sample and at other points in the deposition[69-71]. It can show us in real time how the deposited material interacts with the sample surface. RHEED operates by using a high-energy electron gun that is directed at the sample position at very shallow angle[69-71]. These electrons interact with the surface atom and scatter creating a diffraction pattern. The diffraction pattern offers great information on the arrangement of atoms on the surface[69-71]. RHEED reveals the quality, crystallinity, and growth characteristics of thin films. The spacing and intensity of the diffraction spots can indicate whether the surface is well-ordered or has defects, such as dislocations[69-71]. RHEED provides immediate feedback on the growth rate and surface morphology. This capability makes RHEED an important tool in many fields for high-quality material synthesis.

2.2.5 XPS

XPS is a powerful surface-sensitive analytical technique used to investigate the elemental composition, chemical state, and electronic environment of materials. XPS operates by irradiating the material's surface with a focused beam of X-rays, which have enough energy to cause the ejection of core electrons from the atoms present at or near the

surface[63, 68]. XPS is used to measure the binding energies by measuring the kinetic energy of the ejected electrons. The binding energies of electrons are unique to each element and are influenced by the electronic state of the atom. The data from XPS generates a spectrum providing information on the material's surface[63, 68]. The XPS spectrum reveals the elements and their chemical states that are present on the surface such as oxidation or types of chemical bonds[63, 68]. It can also provide information on whether the atoms are part of a molecule or ion[63, 68]. XPS works within a range of 1 to 10 nm which makes it ideal for studying surface phenomena, such as corrosion, adhesion, and catalysis. Figure 2.10 illustrates an XPS operation.

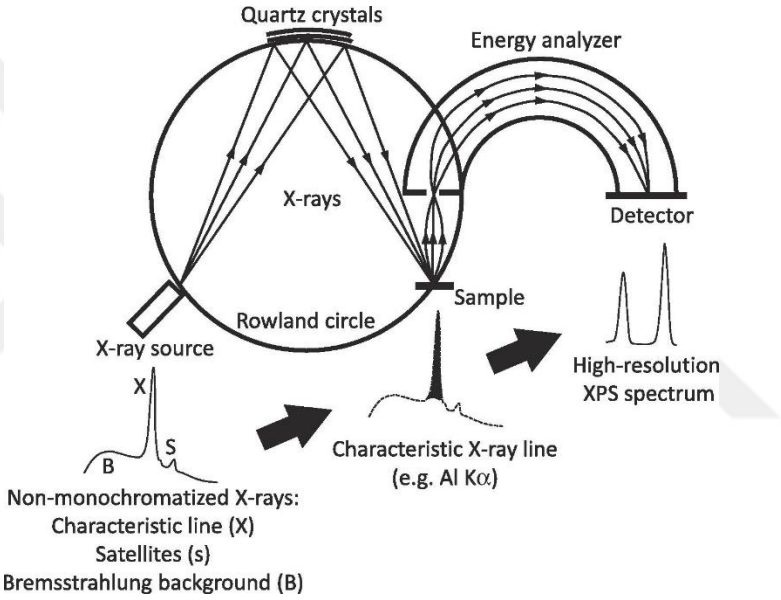

Figure 2.10: Schematic illustration of the principle behind X-ray monochromatization[68] with permission from Elsevier.

2.2.6 Raman Spectroscopy

Raman spectroscopy is an ideal technique used to gain insight into the composition, structure, and interactions within a material. Raman spectroscopy works by directing a laser with a 90-degree angle at the sample being analyzed[62,63]. Information on the material is gained from the scattered laser light due to the interaction of the incident laser with the atoms in the sample[17,18]. The scattered laser light is shifted to different wavelengths due to its interaction with atomic vibrations — this phenomenon is called Raman scattering [17,18,62,63]. A Raman spectrum is generated from the energy level shift which provides a unique molecular fingerprint of the sample[62,63]. The spectrum reveals characteristic peaks

of the material, allowing for the identification and characterization of its chemical composition and structure. It is a non-destructive technique that requires minimal sample preparation.

Chapter 3:
MBE EXPERIENCE

This chapter is meant to highlight my experience with the MBE system, from its initial installation to its successful operation. This chapter is divided into different sections highlighting the different steps and components in the operation of the MBE system. First, the chapter will cover the steps for the installation of the MBE system. Following this, it will cover effusion cells. The discussion will include their operation, and impact on the process. Next, the chapter will cover the electron-gun and its operation. In addition, the chapter will cover the different components of the growth stage and highlight its crucial role in the deposition process. Moreover, this chapter will cover different other components like the ion pump, the rough pump, and the cryogenic pump. Each of these components plays an important role in keeping the UHV environment needed for a successful MBE deposition. This chapter aims to provide an understanding of both the technical and practical elements involved in operating and maintaining the MBE system effectively.

3.1 MBE System Installation

Figure 3.1 provides a picture of the MBE system, showing the different components that will be discussed in this chapter. The MBE chamber is located in the foreground of the picture. The transfer chamber is directly behind the MBE chamber. It ensures that samples can be moved from on part of the system to another without disruption of the UHV environment. Above the transfer chamber we can see the load lock which the starting point of an MBE process is used to introduce samples to the system without disruption of the UHV in the other chambers. In the back of the image is the sputtering chamber which will be utilized to complement the MBE processes. The initial step was to make sure that all the three parts of MBE, Transfer chamber, and sputtering chamber are connected securely making sure the gaskets are well secured in the connecting flanges. The vacuum in the load lock is established with a two-step process of firstly the rough pump and secondly with the turbo pump. These components will be shown later in this chapter. The load lock is pumped independent of the other parts. The next step was to connect the chiller to the effusion cells and the helium compressor necessary for the operation of the cryogenic pump. The next step involved connecting the power supplies to the effusion

cells and the stage heater. By completing these setup tasks, the MBE system was prepared for its operational phase.

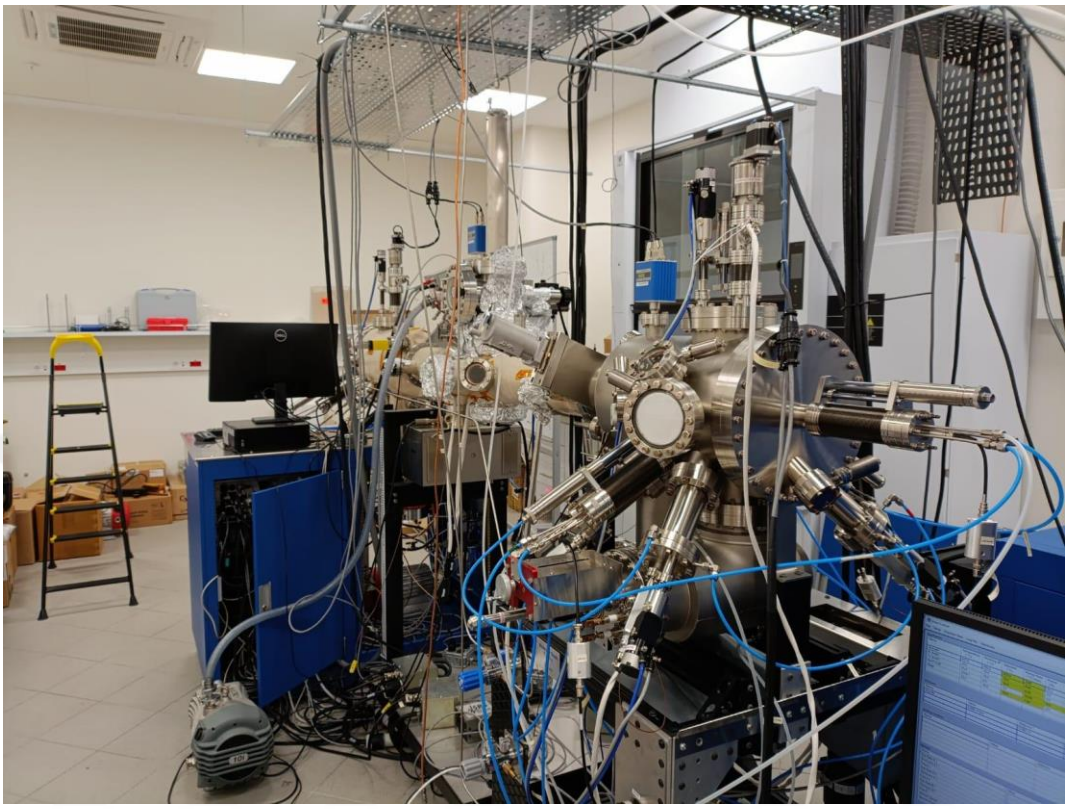

Figure 3.1: Our MBE System.

A typical deposition process within the MBE system begins with loading the samples into the load lock chamber. The load lock must first be vented to atmospheric pressure. After loading the samples on the sample holders into the load lock it is then pumped out to achieve a pressure level comparable to that of the transfer chamber. The sample holders are placed in a mechanical elevator that lowers them into the transfer chamber where they are placed on the transfer arm. Following this, the mechanical elevator is retracted back into the load lock, and the gate valve separating the load lock from the transfer chamber is securely closed to maintain vacuum integrity. The transfer arm is then utilized to move the sample holder from the transfer chamber to the MBE chamber. It is crucial to ensure that the pressure in the transfer chamber is comparable to that in the MBE chamber before opening the gate valve separating the two chambers. This step prevents contamination or disruption of the vacuum conditions. Once the gate valve between the transfer chamber and the MBE chamber is opened, the transfer arm carefully positions the sample holder

onto the growth stage within the MBE chamber. After the sample holder is correctly aligned on the growth stage, the transfer arm is retracted back into the transfer chamber.

3.2 Effusion cells

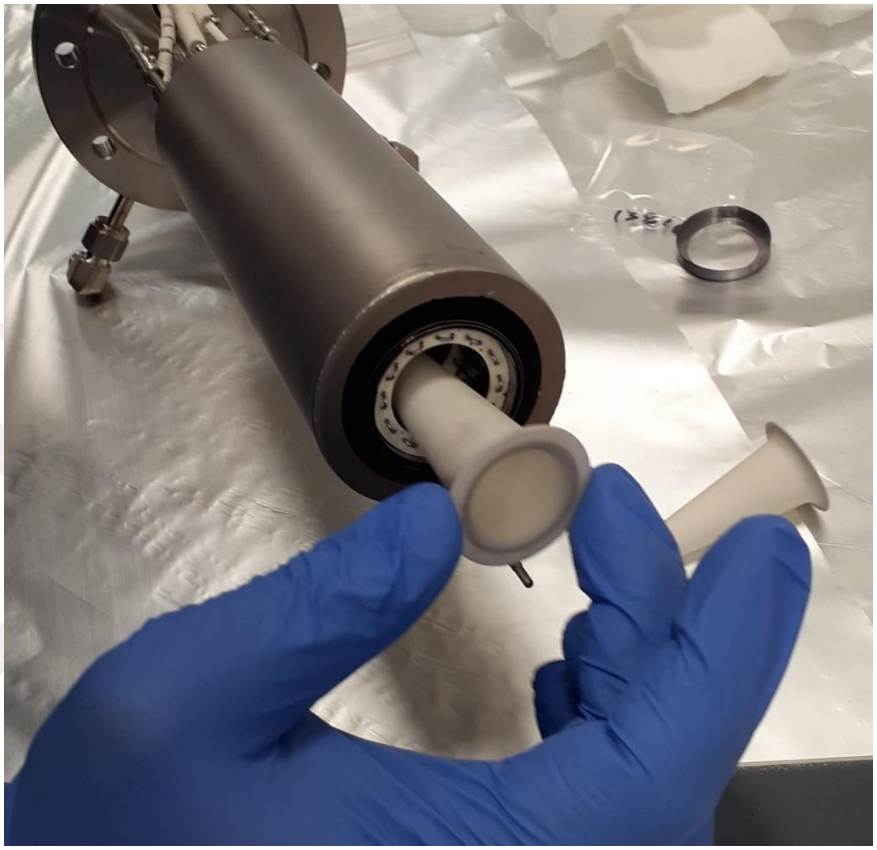

Figure 3.2: a picture of one of the effusion cells used in our MBE system.

Figure 3.2 provides a view of one of the effusion cells used in the MBE chamber. Effusion cells are loaded with source material and are heated up to generate beams if atoms that are directed at the substrate. The atoms adsorb on the surface of the substrate and follow the crystal structure of the substrate. The effusion cell is protected by an encasing shroud to ensure degassing does not disrupt the chamber's environment. The material evaporation is done using ohmic heating using heating filament coils that can be identified in the inner white circle in Figure 3.2. These coils span the entire length of the crucible, providing uniform heating along the effusion cell. The crucible shown in the figure is positioned at the center of the effusion cell. The crucibles are typically made of pyrolytic boron nitride. The effusion cells are equipped with a pneumatic shutter to control the deposition flow. At the bottom of the effusion cell, we can see the water-cooling inlet and outlet pipes. Our MBE system holds 4 effusion cells with one of them being a high

temperature cell. All effusion cells have their own heater power supplies. This figure illustrates the essential components and setup of the effusion cell, emphasizing the roles of the heating filament, shutter mechanism, and water-cooling system in the MBE deposition process.

3.3 Electron gun

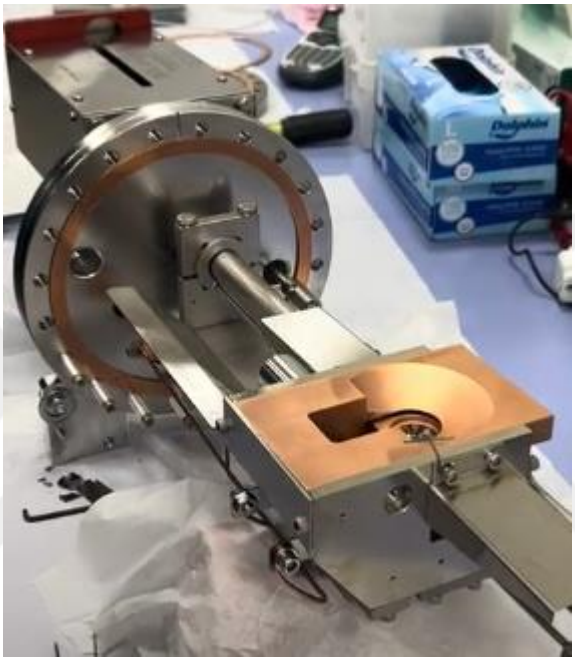

Figure 3.3: a picture of the electron gun material tray.

Electron-gun deposition is used in many different applications. The system in which the electron-gun is used provides high-voltage electric current, typically ranging from 5 to 10 kilovolts (kV). This current is directed through a tungsten filament which is positioned outside the deposition zone adjacent to the copper crucible. When the filament is heated up it emits electrons through thermionic emission. Permanent magnets are used to accelerate and guide the electrons towards the source material. The target material sits in the crucible which is water-cooled. When the electrons strike the target material, they transfer its energy to it causing it to heat up. This causes the target material to evaporate. Once evaporated, the material forms a vapor that rises through the vacuum chamber towards the substrate. Additionally, our electron gun system is equipped with a carousel mechanism making it ready to hold up to five different source material. Electron beam

evaporation is particularly valuable for depositing materials with high melting points, as it can achieve the high temperatures required for their evaporation.

3.4 Growth stage

Figure 3.4: a picture of the bottom of the growth stage showing the heater coil and the rotation gears.

Figure 3.4 provides a detailed view of the growth stage as it is positioned within the deposition chamber. The growth stage is equipped with two hinges, visible in the figure, that hold the substrate holder and allow the rotation of the sample holder. The heating coil is positioned at the center of the growth stage as can be seen in Figure 3.4. The heating coil is connected to its own independent heater and is used to control the temperature of the substrate before, during, and after the deposition process. Substrate temperature control is essential to ensure the desired properties of the thin film being deposited. The

heating of the substrate essentially provides energy for the incoming atoms to arrange themselves on the substrate surface in a uniform manner which depends in the material used. Additionally, the growth stage is fitted with a pneumatic shutter, which adds another layer of control to the deposition process. The stage also has a manual height adjuster positioned outside of the chamber. Overall, Figure 3.4 highlights the different parts of the growth stage within the deposition chamber. The combination of rotational hinges, heating coil, pneumatic shutter and height control ensures that the stage can be controlled precisely to suit the deposition needs.

3.5 Vacuum pumps

Different types of pumps are utilized to ensure the high vacuum environment for thin film deposition. We have a combination of rough pump and a turbo pump for the load lock. The rough pump is used to initially evacuate the load lock as a first stage towards high vacuum. The range of the rough pump is above $1x10^{-3}$ torr. Pumps that operate in high vacuum typically operate inefficiently at atmospheric pressure and that is where the turbo pump comes. Turbo pump works on the principle that gas molecules can be given momentum in a desired direction by repeated collision with a moving solid surface and eventually reaching the exhaust[72]. The transfer chamber is kept under ultra-high vacuum using an ion pump. An ion pump operates without moving parts or fluids, using an electrical discharge within a magnetic field to generate a dense swarm of fast-moving electrons known as plasma[73-75]. These electrons collide with gas molecules, ionizing them and creating positive ions. When these ions strike the cathode, they sputter the cathode material atoms, which is typically titanium, from the cathode's surface, embedding them into the cathode and forming a getter film on the anode, cathode, and inner walls of the pump[73-75]. This getter film, composed of chemically active cathode material, adsorbs surrounding gas molecules as it forms. Gasses like hydrogen, oxygen, nitrogen, carbon monoxide, and inert gases such as helium are ionized and either embedded in the cathode or captured by the getter atoms[73-75]. This process reduces the number of gas molecules in the environment, effectively creating an ultra-high vacuum. Next is the cryogenic pump that is used for the MBE chamber. A cryogenic pump utilizes extremely low temperatures to create and maintain ultra-high vacuum[76]. This is done by cooling a series of surfaces to cryogenic temperatures, typically using helium, which causes the gasses to condense

and solidify onto these surfaces[76]. When gas molecules come into contact with the cold surfaces, they lose a significant amount of their energy, causing them to solidify and consequently reducing the number of gas molecules in the vacuum chamber[76]. The cryogenic pump has multiple stages with progressively colder temperatures to capture a wide range of gasses[76]. The cryogenic pump is connected to a helium compressor which is in turn connected to the system`s chiller. Both the ion pump and the cryogenic pump cannot work efficiently at atmospheric pressures for the chamber sizes we have so getting to ultra-high vacuum in the transfer and MBE chamber follows a process with multiple steps. The gate valve between the transfer chamber and the MBE chamber as well as the gate valve between the transfer chamber and the load lock need to be opened first. The combined system is then pumped down using the combination of the roughing pump and the turbo pump as an initial step to reach high vacuum. Once the pressure is around 10^{-6} torr in the MBE chamber the cryogenic pump is turned on for regeneration. Typically, this process takes around a couple of hours. The gate valve of the cryogenic pump is kept closed at this point. Once the cryogenic pump temperature reaches levels lower than 10 K, the gate valve of the cryogenic pump is opened, and a sudden drop of pressure is observed on the pressure gauge of the MBE chamber. The gate valve separating the transfer and MBE chambers is then closed. The transfer chamber goes through a similar process however the regeneration process of the ion pump goes through and on/off phases of 5 minutes intervals for 30 minutes before reaching the desired pressure values which at that point the gate valve to the load lock is closed. Figure 3.5 shows the cryogenic pump we use in our lab and Figure 3.6 shows the turbo pump and rough pump.

Table 3.1: working range of different types of pumps. It's important to note that for turbo pump, the size of the pump affects the working range.

Pump	Rough pump	Turbo pump	Ion pump	Cryogenic pump
Working range	1 Torr – 10^{-3} Torr	10^{-4} – 10^{-8} Torr	10^{-9} – 10^{-12} Torr	10^{-9} – 10^{-12} Torr

Figure 3.5: Cryogenic pump.

Figure 3.6: Turbo pump (left), and rough pump (right).

Chapter 4:

BI_2TE_3 AND SB DOPED BI_2TE_3

The introduction chapter of this thesis explores the significance of growing and the characterizing Bi_2Te_3 and its doped variants. It details the growth processes and characterization techniques used for the Bi_2Te_3 thin films we produced. All samples were grown using an MBE system on sapphire substrates, with the MBE chamber maintained at an ultra-high vacuum of approximately 10^{-9} torr throughout the growth processes. The chapter outlines the multi-phase approach of our growth process. The first phase involved film optimization, focusing on calibrating deposition parameters to achieve the desired stoichiometry of Bi_2Te_3 in the second phase, we conducted a thickness-driven study of Bi_2Te=, examining the effects of varying growth times on film properties. The third phase introduced doping of the Bi_2Te_3 films with Sb to investigate how different doping levels affect the thin films. To characterize the films, the chapter will present data from XRD and XPS, among other techniques, to provide a comprehensive understanding of the structural and compositional properties of the samples. Figure 4.1 shows a depiction of the growth kinetics of the Bi_2Te_3 and Sb doped Bi_2Te_3.

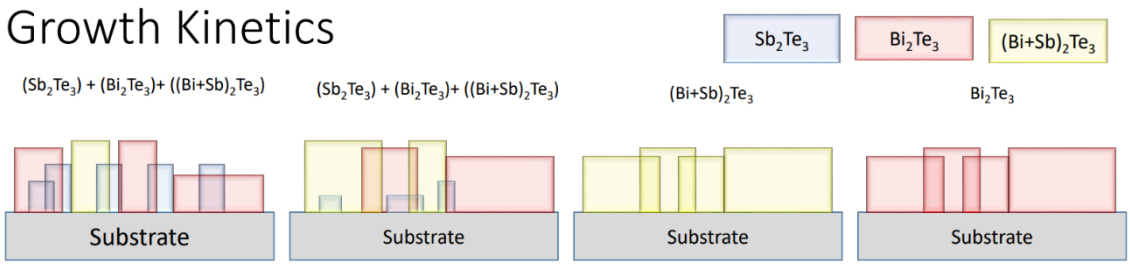

Figure 4.1: Growth kinetics depiction of our samples.

4.1 Optimization phase

We began our growth process with a calibration period to fine-tune the deposition rates of Bi and Te. Initially, we set the growth temperatures at 650 °C for Bi and 412 °C for Te, with the substrate stage temperature fixed at 230 °C. Our first attempt to grow a film lasted 90 minutes, but it resulted in no coverage on the substrate. To address this issue, we adjusted our parameters and increased the growth time to 120 minutes while lowering the Bi effusion cell temperature to 540 °C. Despite these changes, the second film also showed no coverage, which prompted further investigation. We then tried a growth at

room temperature for the substrate stage, maintaining the Bi effusion cell temperature at 540 °C, for 60 minutes. This adjustment led to the first observable growth on the substrate, though the film was non-homogeneous and appeared cloudy. This partial success provided valuable insights into the potential issues with our earlier attempts and guided us in refining our growth conditions.

Following the above results, we went into a series of growth attempts for calibration that were based on the change of growth stage temperature. We attempted the deposition for 2 substrates keeping Bi Effusion cell temperature at 550 °C and Te effusion cell temperature at 412 °C. We suspected that the addition of a post annealing step could enhance the film`s homogeneity. The first sample had a stage temperature setpoint of 50 °C for 120 minutes of growth time and a post annealing at 100 °C for 60 minutes. This sample showed a homogeneous cloudy thin growth. The post annealing could have been the cause of the homogeneity and the low thickness of the film, but it was still far from the features we are looking for. We suspected that the low stage temperature set point could be the culprit for the cloudy look that our thin film had so for the second sample we increased the stage temperature set point to 100 °C and we did not do any post annealing. This sample showed a thicker homogenous but cloudy film. Due to the previous results we decided to re-calibrate the stage temperature heater and we noticed that the setpoint and actual temperature are off so for all the next growth we followed the power curve of the stage heater to properly set the stage temperature. Our previous investigation led us to the same conclusion we made from the stage temperature heater power curve. We deposited 2 samples following that. For the first sample we had the stage temperature at 190 °C. This is close to previously reported successful growth in research papers and it is around the actual temperature where our samples showed any homogenous growth. For this sample we increased the Bi effusion cell temperature to 665 °C to increase the Bi rate. The growth was done for 90 minutes. This sample showed a stoichiometry of Bi_4Te_3 which was promising because it meant that we are on the right track to reach the desired stoichiometry. The second sample was to confirm the Bi rate change effect on the film quality. For this sample we decreased the Bi effusion cell temperature to 550 °C but in compensation we increased the growth time to 150 minutes. This sample showed the same stoichiometry of Bi_4Te_3. The lowering of Bi effusion cell temperature was done to conserve material and elongate the lifetime of it. From here we

decided to increase the stage temperature to 205°C to see the effect it has on the stoichiometry. This growth was for 60 minutes like the previous sample. At las we managed to get a reflective thin film with the desired stoichiometry of Bi_2Te_3. The XRD data of sample AO280224 in Figure 4.2 shows the characteristic peaks for Bi_2Te_3 however we noticed a high-intensity secondary in-plane reflection at the (015) plane.

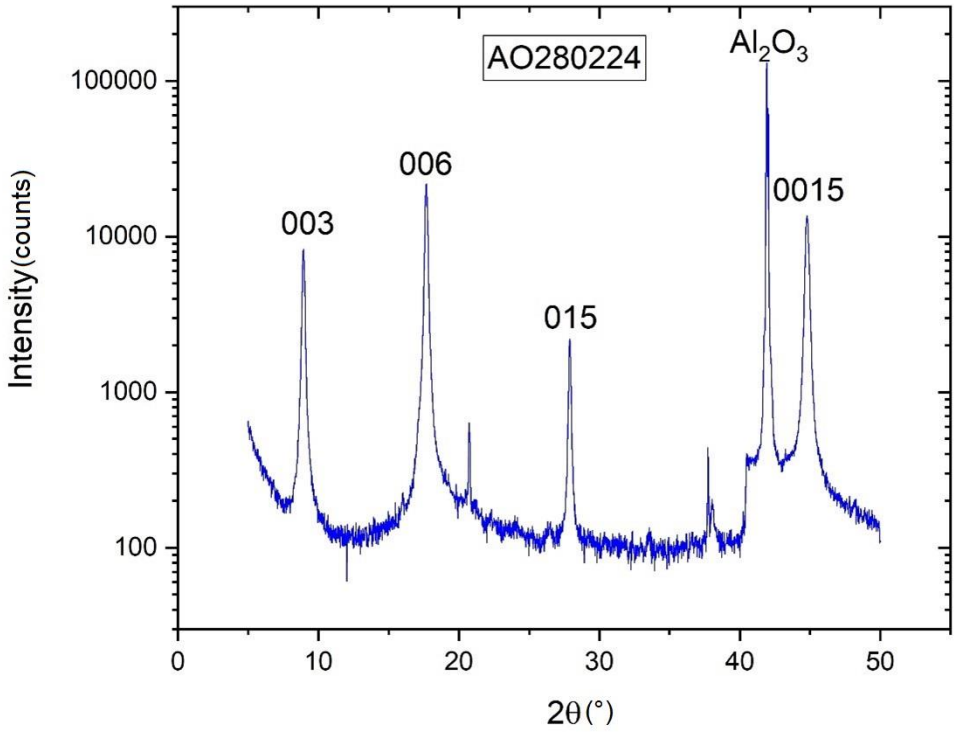

Figure 4.2: XRD data for the first successfully grown Bi_2Te_3 thin film (measurements done by Aykut Can Onel and analysis by Ahmad El Zatari).

In response to the secondary in-plane reflection observed in our previous sample, we aimed to adjust our growth parameters to suppress this reflection. We prepared a new sample, maintaining a consistent deposition time of 60 minutes. For the second sample, named AO110324, we adjusted the Bi effusion cell temperature to 535 °C and the Te effusion cell temperature to 417 °C, while keeping the stage temperature at 205 °C. Both sample AO280224 and sample AO110324 underwent a post-annealing process at 100 °C for 60 minutes. We included the post-annealing step in our protocol to improve the quality of the Bi_2Te_3 films, based on the positive results obtained with previous samples. The XRD analysis of these two samples, as shown in Figure 4.3 for comparison, indicates that

the secondary in-plane reflection has been significantly reduced in the second growth. This reduction suggests that the adjustments in the effusion cell temperatures and the application of the post-annealing step contributed to mitigating the unwanted reflection, thereby improving the overall quality of the Bi_2Te_3 films.

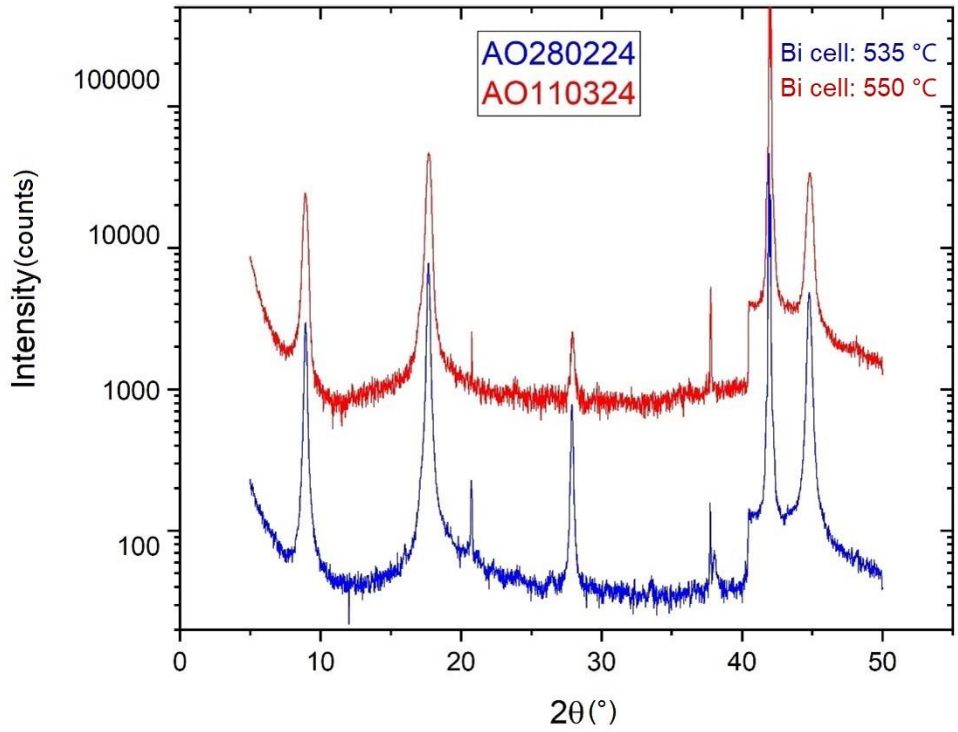

Figure 4.3: XRD data showing the secondary in-plane reflection peak intensity change based on growth parameters change as shown (measurements done by Aykut Can Onel and analysis by Ahmad El Zatari).

Lowering the Bi effusion cell temperature and increasing the Te effusion cell temperature led to a decrease in the Bi deposition rate and an increase in the Te deposition rate. These changes allowed for a more balanced incorporation of both elements into the film, which contributed to the decreased intensity of the secondary in-plane reflection peak. Additionally, the presence of fringes around the Bragg peak in the XRD patterns suggests a high degree of coherence between the film surface and the substrate surface, indicating improved film quality and alignment.

4.2 Thickness study

Observing the changes from the previous X-ray Diffraction (XRD) data, we decided to investigate how varying film thicknesses might affect the intensity of the secondary in-plane reflection peak. To explore this, we adjusted the deposition time while keeping all other parameters constant. For the first sample, we set the Bi effusion cell temperature to 535 °C the Te effusion cell temperature to 417 °C, and maintained the growth stage temperature at 205 °C. We started with a 60-minute growth time. Figure 4.4 shows the XRD data of the thin film. We can see the characteristic peaks of Bi_2Te_3 with corresponding planes of (003) and (006). This film exhibits a very low intensity of the secondary phase at (015) plane. This film was homogenous of high-quality with metallic features apparently present. Using XRR the thickness of this film was found out to be 13 nm. The full width half maximum (FWHM) of the 006 peak is calculated to be 0.573 which corresponds to a crystalline size of 14 nm which correspond to our XRR data of the thin film.

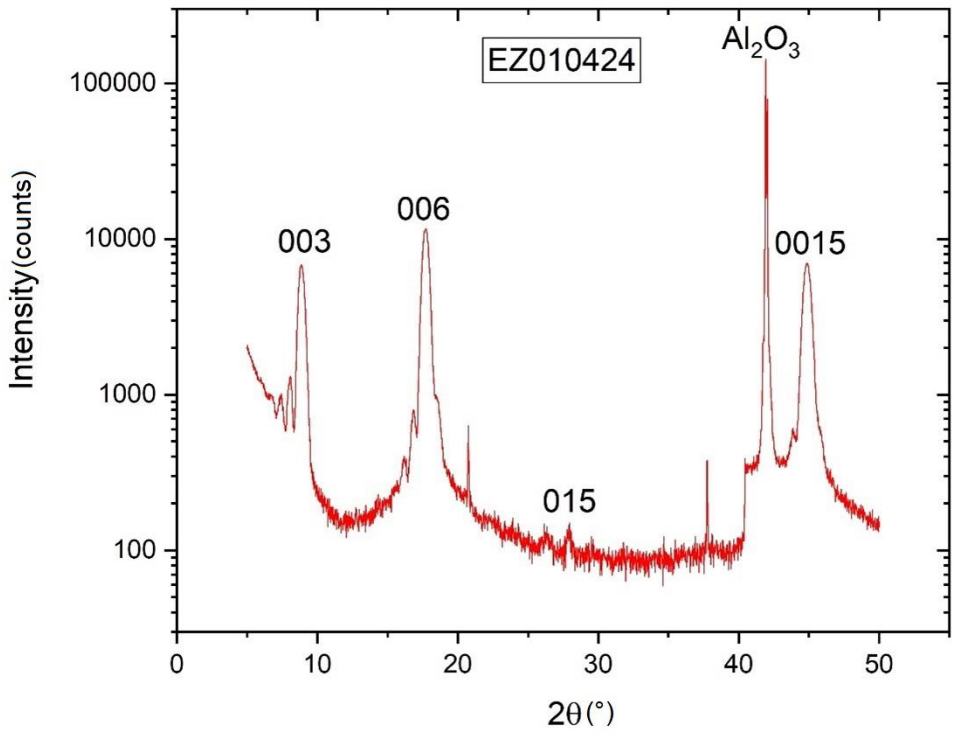

Figure 4.4: XRD results of thin film EZ010424 (Measurements done by Ebrahim Zahrabi and analysis by Ahmad El Zatari).

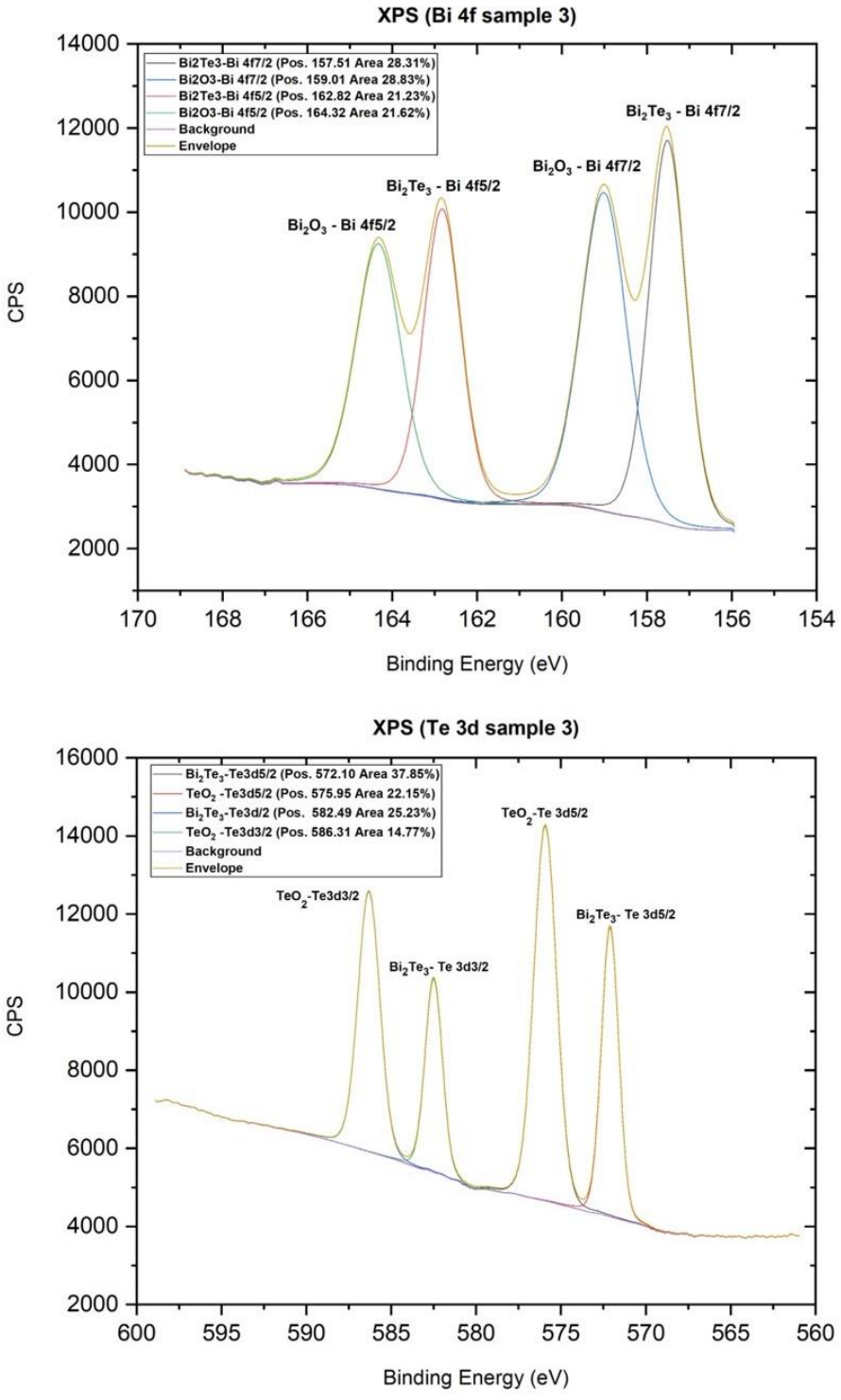

Figure 4.5 XPS results for thin film EZ010424 (Measurements done by Baris Yagci).

The XPS results for sample EZ010424 shown in Figure 4.5 show the Bi 4f and Te 3d peaks that are consistent with literature. These results are a confirmation of the quality of the film.

Figure 4.6 shows the XRR results for sample EZ010424. We can see the Kiessig fringes apparent in the graph indicating a proper read of the thickness and roughness of the thin film.

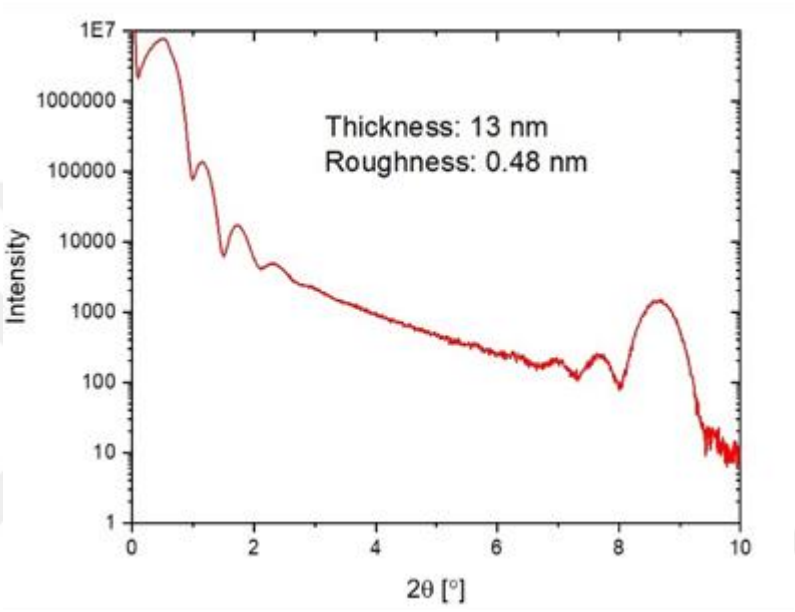

Figure 4.6: XRR results for thin film EZ010424 (Measurements done by Aykut Can Onel).

For the second sample named EZ030424, we kept the Bi effusion cell temperature, Te effusion cell temperature, and the growth stage temperature at the same values as sample EZ010424. We changed the growth time to 90 minutes. Figure 4.7 shows the XRD data of the thin film. We can see the characteristic peaks of Bi_2Te_3, and we can see a higher intensity of the secondary phase at (015) plane. This thin film had a cloudy inhomogeneous look to it. It is presented here to further support that the proper refinement of growth parameters is crucial for a high-quality, low-intensity secondary phase films.

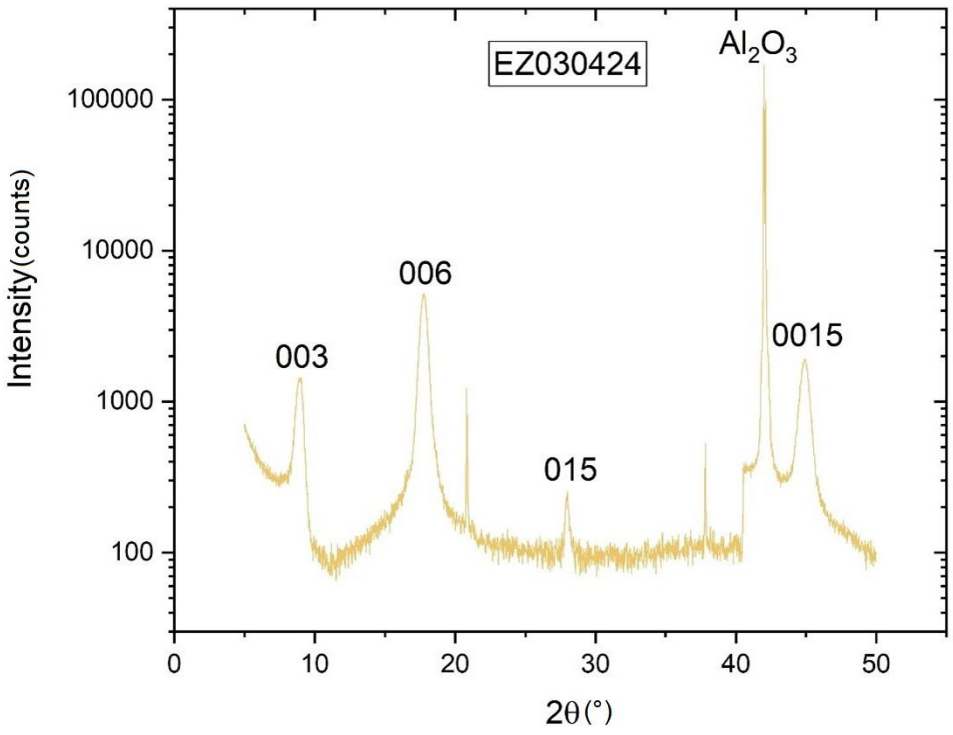

Figure 4.7: XRD results of thin film EZ030424 (Measurements done by Ebrahim Zahrabi and analysis by Ahmad El Zatari).

For the third sample name EZ040424, we kept the Bi effusion cell temperature, Te effusion cell temperature, and the growth stage temperature at the same values as sample EZ010424. We changed the growth time to 120 minutes. The XRD data for this sample, as depicted in Figure 4.8, shows the relative intensity of the secondary in-plane reflection peak compared to the 006 peak. The FWHM of the (006)-plane peak of this sample is calculated to be 0.268 and a crystalline size of 30 nm. This data provides insights into how the increased film thickness influences the secondary peak intensity, offering valuable information on the relationship between film growth parameters and the structural quality of the Bi_2Te_3 films.

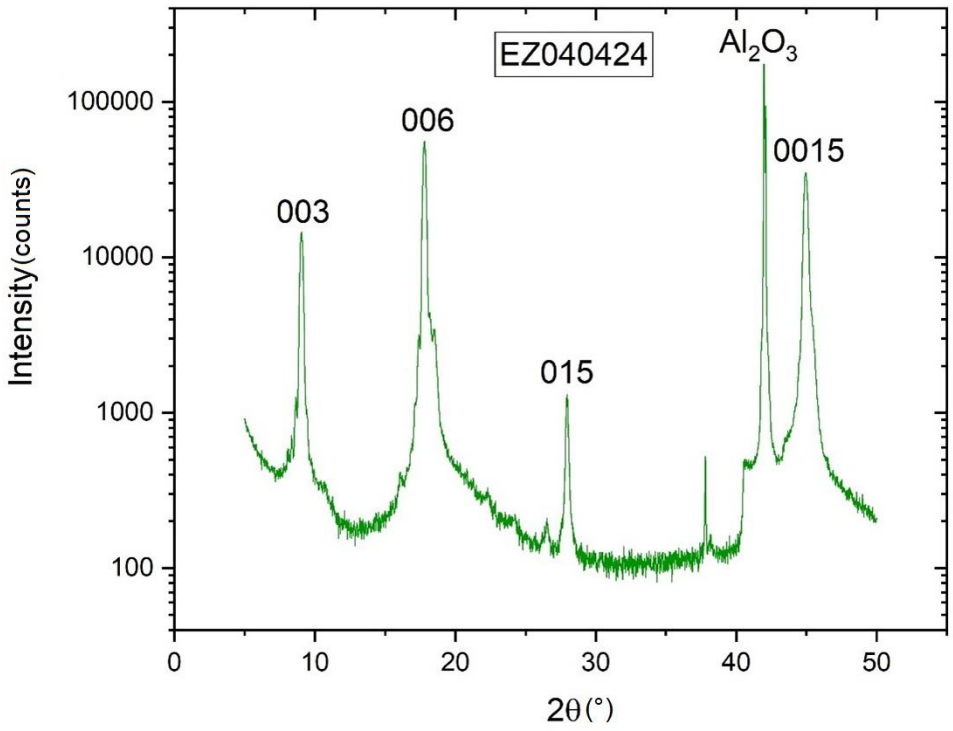

Figure 4.8: XRD results of thin film EZ040424 (Measurements done by Ebrahim Zahrabi and analysis by Ahmad El Zatari).

Table 4.1: A summary table of the recipes for the undoped samples.

	EZ040424	EZ030424	EZ010424
Bi(°C)	535	535	535
Te(°C)	417	417	417
Growth stage(°C)	205	205	205
Growth duration(min)	120	90	60

Our Bi_2Te_3 thin films show characterization results consistent with literature. However, in this thesis we provide multiple different ways to suppress the secondary in-plane peak which is a topic that is not well explored. This paves a way for higher-quality films which would benefit doping cases heavily.

4.3 Sb doped Bi_2Te_3

After the thickness study we decided to start doping the Bi_2Te_3 thin films. In this subsection we will discuss multiple samples and their characterization results. We expected the presence of the secondary phase peaks in the doping process as well, so the aim of this study was to try and suppress the secondary phase with doping.

The first sample name EZ220424 was grown with Bi effusion cell temperature of 535 °C, Te effusion cell temperature of 417 °C, and Sb effusion cell temperature of 455 °C. The growth stage temperature was kept at 205 °C similar to the non-doped samples. Figure 4.9 shows the XRD results for this sample. Due to symmetry (009), and (0012) are not allowed. Sb doping may break the symmetry and unallowed reflections are now allowed. the two phases develop together from start till the end of the growth at high Sb cell temperature.

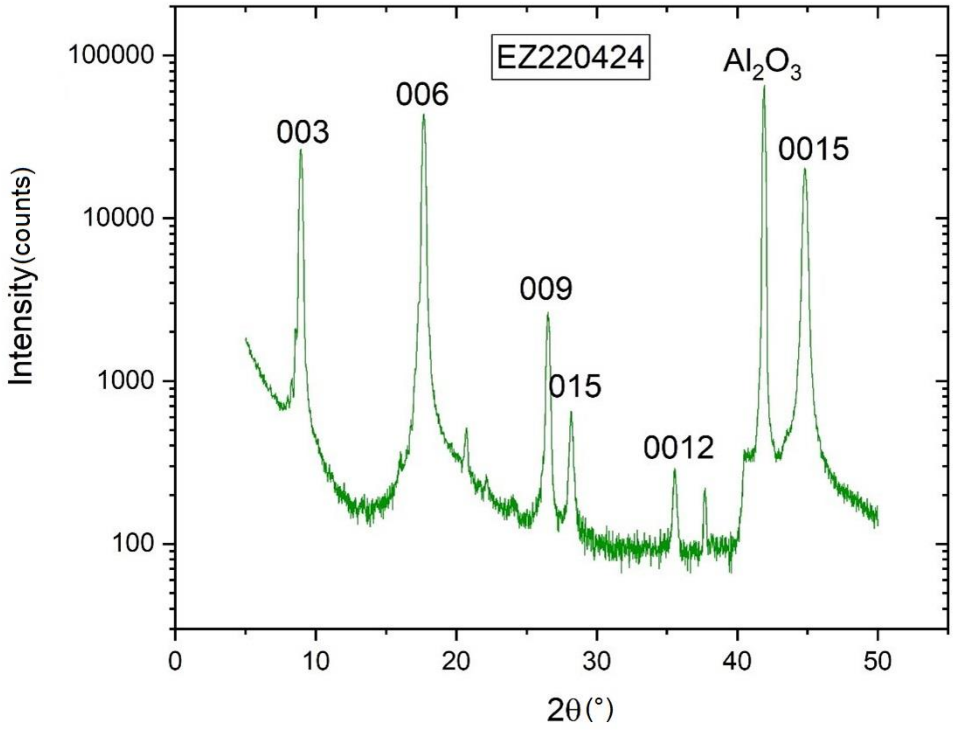

Figure 4.9: XRD data for thin film EZ220424 (Measurements done by Ebrahim Zahrabi and analysis by Ahmad El Zatari).

The second sample named EZ250424 had similar growth parameters except the reduction of Sb effusion cell temperature from 455 °C to 450 °C. The aim of this temperature reduction was to see the effect of it on the secondary phase intensity. Figure 4.10 shows the XRD results of this sample. This sample had a cloudy inhomogeneous look to it. This can be understood from the intensities of the identifying peaks of our thin films as well as the relative ratio of the secondary phase peak to the identifying peaks.

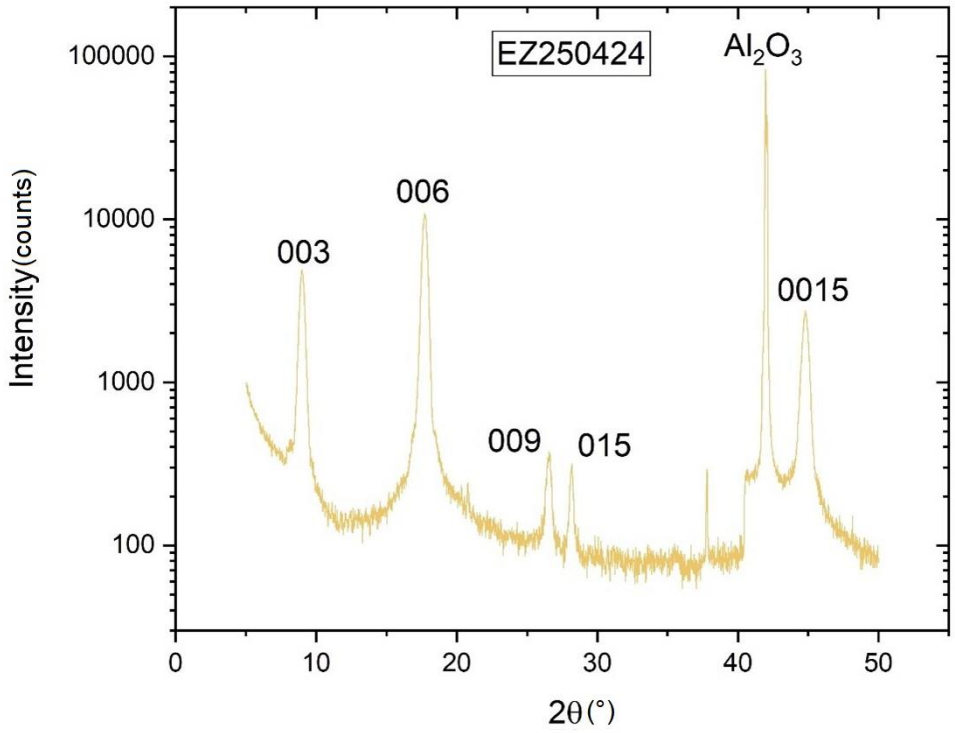

Figure 4.10: XRD results of thin film EZ250424 (Measurements done by Ebrahim Zahrabi and analysis by Ahmad El Zatari).

The third film named EZ260424 had another Sb effusion cell temperature reduction of 5 C making it 445 °C. Figure 4.11 shows the XRD results of this sample. This film was a homogeneous film with metallic features indication the success of this growth. When we compare this film to EZ220424 we can see a significant decrease in the intensity of the secondary phase while the identifying peaks showed a relatively small decrease in intensity. This was an indication that our approach to suppress the secondary phase has worked. It is important to note the fringes around the Bragg peaks as an indicator of a high-quality film.

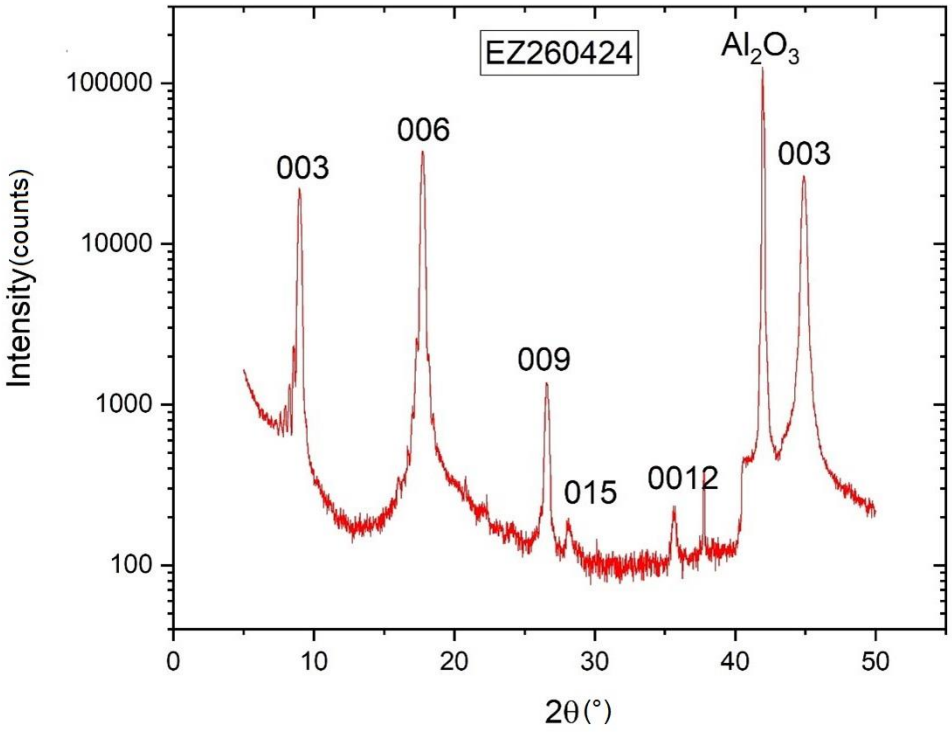

Figure 4.11: XRD results of thin film EZ260424 (Measurements done by Ebrahim Zahrabi and analysis by Ahmad El Zatari).

According to the XRD data, the thickness nearly doubles when Sb is added under the identical growth condition to non-doped samples. Sb should incorporate into the crystal rather than generate a separate phase. Figure 4.12 shows a focused view on the XRD data of multiple of our doped samples. We can see a continuous drop in Sb_2Te_3 (009) and (0012) peaks intensity as Sb cell temperature decreases. This indicates the inclusion of Sb into the lattice. The film's thickness eventually approaches that of pure Bi_2Te_3 growth.

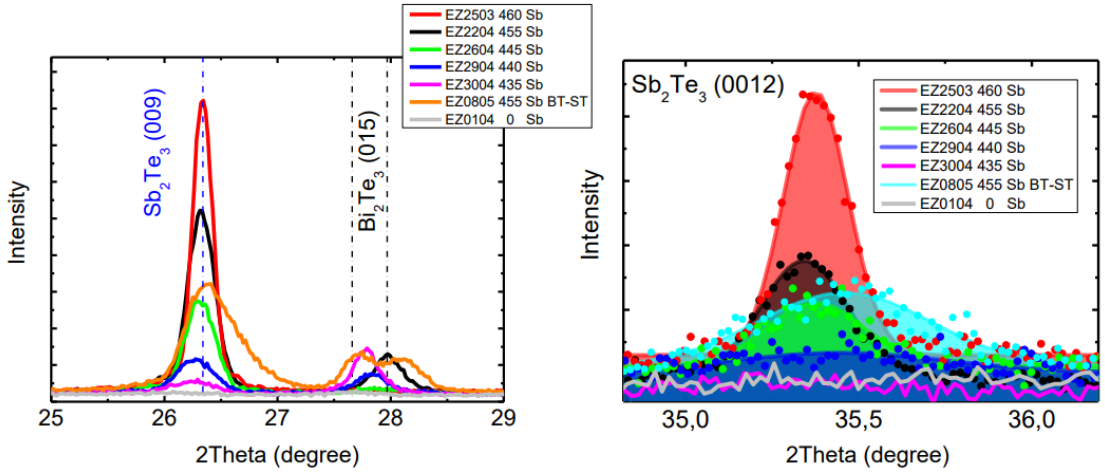

Figure 4.12: A focused view on the XRD results of multiple doped films and a reference film (Measurements done by Baris Yagci).

Figure 4.13 shows the XPS Bi 4f peaks comparison between the doped thin films discussed above and the EZ010424 Bi_2Te_3 film. We can see the shifts of the binding energy with each sample grown where EZ260424 shows the highest shift. Lowering of the Sb shows a better incorporation of Sb into the lattice.

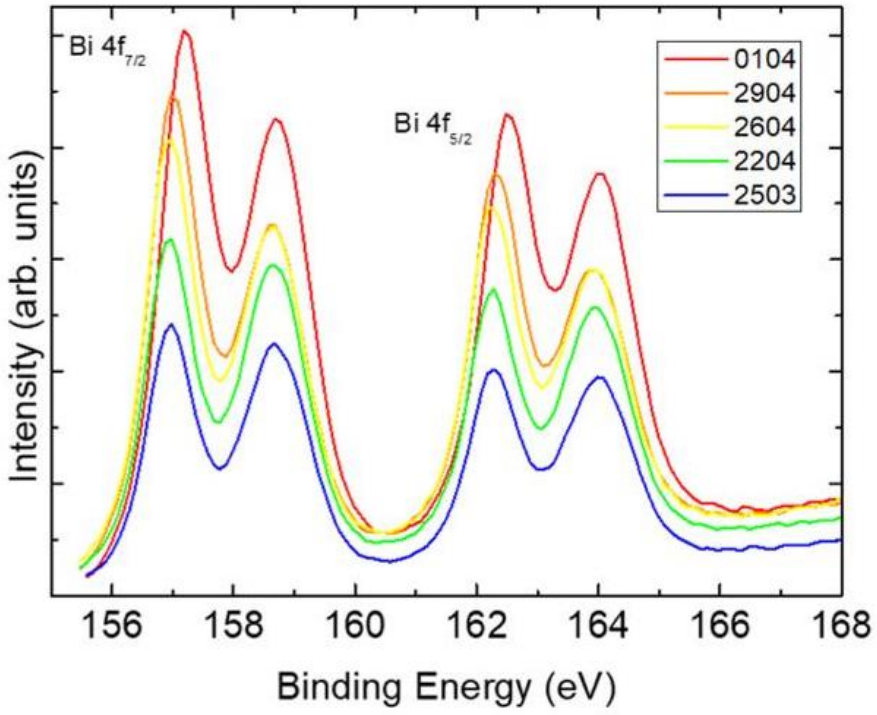

Figure 4.13: XPS peaks comparison (Measurements done by Baris Yagci).

To add to further to the point made in Figure 4.13 we have Figure 4.14 showing the Bi 4f peak shift and the Te 3d peak shift with respect to Sb effusion cell temperature. We can see from Figure 4.14 that there is a difference in shifts when the Sb effusion cell temperature is above 445 ℃ which is explained by the presence of Sb_2Te_3 phase due to

the high rate of Sb. However below 445 ℃ we see that the shifts are in line with each other indicating better incorporation of Sb into the underlying lattice which agrees with the XRD results shown in Figure 4.12. These results also complement the illustration in Figure 4.1. Table 4.2 shows a summary of the recipes showcased in the doping section.

Table 4.2: recipes of the films discussed.

	EZ250424	EZ250424	EZ260424
Bi(°C)	535	535	535
Te(°C)	417	417	417
Sb(°C)	455	450	445
Growth stage(°C)	205	205	205
Growth duration(min)	60	60	60

Our samples show similar characteristic peaks to the literature, whether it is pure Bi_2Te_3 or Sb-doped Bi_2Te_3[77-90]. However, there are still some differences that depend on multiple factors. In some cases, for Bi_2Te_3, we can see that the (015) dominates the XRD pattern[80, 81, 83]. For the Sb-doped Bi_2Te_3 we can see the (015) peak dependence on the deposition parameters from working pressure to Sb concentration[86, 88]. In 78, The Bi_2Te_3 deposition was approached from the opposite direction to what we did in our work as in the temperatures were in an increasing order from 350 ℃ to 450 ℃. The increase in temperature of the Bi_2Te_3 sputtering target used caused the suppression of the (015) peak[78]. This work doesn't dive into more detail on the individual temperature effect on the secondary phase since the source is a Bi_2Te_3 sputtering target. One thing that needs to be mentioned is that there is a gap in the literature where the effects of this secondary phase and the possible ways of suppressing it are not well studied. Our work dives deeper into the different ways the secondary phase can be suppressed, and it shows the individual effects of parameters changes of the different sources at play. Current and future work will go into the effects of it on the transport properties.

Chapter 5:
CONCLUSION AND FUTURE WORK

5.1 Conclusion

This thesis has explored the unique properties TIs, focusing on Bi_2Te_3 and its doped variants. TIs are well known their insulating bulk and conducting surface due to the topologically protected surface states, which exhibit a Dirac-like band structure. These surface states show a robustness against perturbations and their spin-momentum locking, making TIs a significant path to work on to realized advancements in quantum computing and spintronics.

Our work highlights the critical role of doping in tuning the electronic properties of Bi_2Te_3 . We showed multiple ways to achieve the suppression of the secondary phase associated with the XRD peak at (015). This work highlights that precise control of growth parameters is essential for achieving high-quality thin films especially for doped variants of Bi_2Te_3 since it is the key to achieving the QAHE. The thickness of the films also plays a crucial role in the observed physics. This research establishes a foundation for band gap engineering of Bi_2Te_3.

Bi2Te3 is favored for its large bulk band gap, robust surface states, and ease of doping, which allow for flexible tuning of its electronic properties. It shows a potential for scalable production due its compatibility with standard semiconductor processing techniques. Additionally, Bi_2Te_3 and its variants are notable for their high thermoelectric performance and unique spin-momentum locking mechanism, which is crucial for spintronic applications.

The process of epitaxial growth of Bi_2Te_3 is essential for producing high-quality films. Techniques such as MBE ensure that films exhibit improved electrical and thermal properties and maintain a well-defined interface with the substrate. Our investigations into various growth parameters and characterization methods have provided valuable insights into optimizing Bi_2Te_3 thin films for advanced technological applications.

Overall, this thesis contributes to the understanding and practical implementation of topological insulators, emphasizing the importance of Bi_2Te_3 in the development of next-generation electronic and spintronic devices.

5.2 Future work

To advance our research on Bi_2Te_3 and doped Bi_2Te_3 thin films, we need to produce films with much lower thicknesses compare to the ones reported in chapter 4-specifically targeting 5 quintuple layers. Achieving this requires meticulous refinement of our current growth recipes to ensue high-quality films. Our future plan will be laid out in the subsections below.

5.2.1 Reproduction and Analysis

Our first task is to reproduce the Sb doped Bi_2Te_3 samples discussed in chapter 4. We will perform ARPES and transport measurements on these samples to understand the effects of the secondary phase in the range of 14 nm to 45 nm. This will provide a base line to our next steps.

5.2.2 Recipe refinement

Based on the measurements and Analysis done in the step discussed above and the illustrated phased diagram of Bi-Te system in Figure 5.1 we will adjust the recipe parameters. Our current samples were grown around 808 K or 535 °C which is a multiple phase region as can be seen from Figure 5.1b. To mitigate the presence of secondary phases and enhance film quality at thinner thicknesses, we need to lower the Bi temperature to around 670 K or 400 °C. This directly causes a need for a change in Te temperature and deposition time. We aim to produce 3 to 5 high-quality, and sub 10 nm Bi_2Te_3 samples.

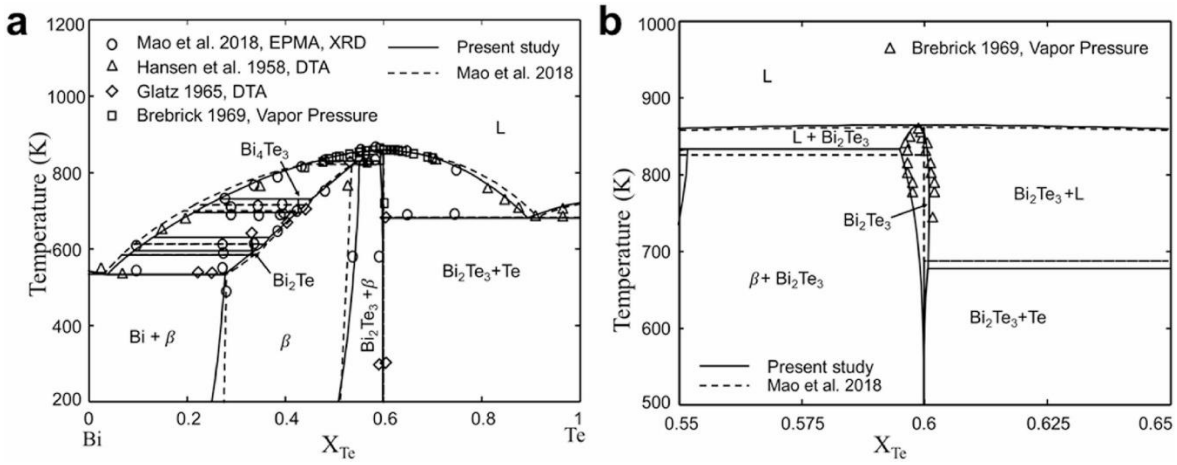

Figure 5.1: (a) Calculated phase diagram of the Bi–Te system[91](b) enlarged homogeneity range of Bi_2Te_3 along with experimental data[91] with permission from Elsevier.

5.2.3 Doping refinement

Upon successful completion of the second step of our plan, we will start doping theses samples. We will first introduce Sb and then V into our Bi_2Te_3 films. we aim to produce high-quality doped thin films at lower than 10 nm thicknesses.

5.2.4 Analysis

All our samples will be analyzed using the techniques discussed in chapter 2 and in addition, we will perform low temperature transport measurements as well as ARPES measurements. Our goal is to understand the impact of the secondary phase discussed in chapter 4 on the transport behavior of the films we are producing. We ultimately want to establish the QAHE in our samples and study it.

BIBLIOGRAPHY

1. Moore JE. The birth of topological insulators. *Nature*. 2010;464(7286):194-198. doi:10.1038/nature08916.
2. Liu Y, Hor YS, Cava RJ, et al. Tuning Dirac states by strain in the topological insulator Bi_2Se_3. *Nature Physics*. 2014;10(4):294-299. doi:10.1038/nphys2898.
3. Nilforoushan N, Garcia H, Schneider WR, et al. Moving Dirac nodes by chemical substitution. *Proceedings of the National Academy of Sciences*. 2021;118. doi:10.1073/pnas.2108617118.
4. Arakane T, Yoshimi R, Sasaki S, et al. Tunable Dirac cone in the topological insulator $Bi_{2-x}Sb_xTe_{3-y}Se_y$. *Nature Communications*. 2012; 3:636. doi:10.1038/ncomms1639.
5. Kou X, Wang KL. Magnetic topological insulators and quantum anomalous hall effect. In: Advances in Quantum Mechanics and Atomic Physics. Springer Singapore; 2019:319-349.
6. Chen X, Ma XC, He K, Jia JF, Xue QK. Molecular Beam Epitaxial Growth of Topological Insulators. *Advanced Materials*. 2011;23(9):1162-1165. doi:10.1002/adma.201003855.
7. Gopal RK, Singh S, Sarkar J, Mitra C. Tuning chemical potential in the Dirac cone by compositional engineering. *AIP Advances*. 2017;7(10):105112. doi:10.1063/1.4999254.
8. Zhang J, Zhang C, Chen X, et al. Band structure engineering in $(Bi_{1-x}Sb_x)_2Te_3$ ternary topological insulators. *Nature Communications*. 2011; 2:574. doi:10.1038/ncomms1588.
9. Zeljkovic I, Zhang X, Lee J, et al. Dirac mass generation from crystal symmetry breaking on the surfaces of topological crystalline insulators. *Nature Materials*. 2015;14(4):318-324. doi:10.1038/nmat4215.
10. Sato T, Nakatsuji S, Nakayama K, et al. Manipulation of Dirac Cone in Topological Insulator/Topological Insulator Heterostructure. *ACS Applied Electronic Materials*. 2021;3(3):1080-1085. doi:10.1021/acsaelm.0c00918.
11. Lee JS, Samarth N, Rispoli M, et al. Engineering the breaking of time-reversal symmetry in gate-tunable hybrid ferromagnet/topological insulator heterostructures. *npj Quantum Materials*. 2018; 3:15. doi:10.1038/s41535-018-0123-2.
12. Krumrain J, Molnar V, Kormos L, et al. MBE growth optimization of topological insulator Bi_2Te_3 films. *Journal of Crystal Growth*. 2011;324(1):115-118. doi: 10.1016/j.jcrysgro.2011.03.008.
13. Kou X, Fan Y, Lang M, Upadhyaya P, Wang KL. Magnetic topological insulators and quantum anomalous hall effect. *Solid State Communications*. 2015;215-216:34-53. doi: 10.1016/j.ssc.2014.10.022.
14. Wiesner M, Mazza M, Schneider C, et al. The effect of substrate and surface plasmons on symmetry breaking at the substrate interface of the topological insulator Bi_2Te_3. *Scientific Reports*. 2019; 9:4571. doi:10.1038/s41598-019-42598-9.
15. Schaibley JR, Yu Y, Mandrus D, et al. Valleytronics in 2D materials. *Nature Reviews Materials*. 2016; 1:16055. doi:10.1038/natrevmats.2016.55.

16. Li R, Xie Z, Zhang L, et al. Robust second-order topological insulators with giant valley polarization in two-dimensional honeycomb ferromagnets. *Nano Letters*. 2023;23(1):91-97. doi: 10.1021/acs.nanolett.2c03680.
17. Li X, Zhang F, Niu Q, Feng J. Superlattice valley engineering for designer topological insulators. *Scientific Reports*. 2014; 4:6397. doi:10.1038/srep06397.
18. Lü XL, Xie H. Spin filters and switchers in topological-insulator junctions. *Physical Review Applied*. 2019;12(6):064040. doi:10.1103/PhysRevApplied.12.064040.
19. Ovchinnikov D, Jeschke H, Liu Y, et al. Topological current divider in a Chern insulator junction. *Nature Communications*. 2022; 13:238. doi:10.1038/s41467-022-33645-7.
20. Chang CZ, Li M. Quantum anomalous Hall effect in time-reversal-symmetry breaking topological insulators. *Journal of Physics: Condensed Matter*. 2016;28(12):123002. doi:10.1088/0953-8984/28/12/123002.
21. Deng Y, Yang H, Zhang J, et al. Quantum anomalous Hall effect in intrinsic magnetic topological insulator $MnBi_2Te_4$. *Science*. 2020;367(6480):895-900. doi:10.1126/science. aax8156.
22. Chang CZ, Zhang J, He K, et al. Experimental observation of the quantum anomalous Hall effect in a magnetic topological insulator. *Science*. 2013;340(6129):167-170. doi:10.1126/science.1234414.
23. Aguado R, Kouwenhoven LP. Majorana qubits for topological quantum computing. *Physics Today*. 2020;73(6):44-50. doi:10.1063/PT.3.4499.
24. Li ZZ, Zhang FC, Wang QH. Majorana modes in a topological insulator/s-wave superconductor heterostructure. *Scientific Reports*. 2014; 4:6363. doi:10.1038/srep06363.
25. Bhattacharyya B, Awana VP, Senguttuvan TD, Ojha VN, Husale S. Proximity-induced supercurrent through topological insulator-based nanowires for quantum computation studies. *Scientific Reports*. 2018; 8:13136. doi:10.1038/s41598-018-35424-1.
26. Cook A, Franz M. Majorana fermions in a topological-insulator nanowire proximity-coupled to an s-wave superconductor. *Physical Review B*. 2011;84(20):201105. doi:10.1103/PhysRevB.84.201105.
27. A voltage-balanced device for quantum resistance metrology. *Nature Electronics*. 2024. doi:10.1038/s41928-024-01168-2.
28. Fijalkowski KM, Frankowski K, Zhang Y, et al. A balanced quantum Hall resistor. *Nature Electronics*. 2024. doi:10.1038/s41928-024-01156-6.
29. Sharma A, Senguttuvan TD, Ojha VN, Husale S. Novel synthesis of topological insulator-based nanostructures (Bi_2Te_3) demonstrating high performance photodetection. *Scientific Reports*. 2019; 9:3804. doi:10.1038/s41598-019-40394-z.
30. Kong D, Cui Y. Opportunities in chemistry and materials science for topological insulators and their nanostructures. *Nature Chemistry*. 2011;3(11):845-849. doi:10.1038/nchem.1171.
31. Liu B, Huang B, Wang J, et al. Surrounding sensitive electronic properties of Bi_2Te_3 nanoplates—Potential sensing applications of topological insulators. *Scientific Reports*. 2014; 4:4639. doi:10.1038/srep04639.
32. Wu H, Chen L, Zhang Y, et al. Magnetic memory driven by topological insulators. *Nature Communications*. 2021; 12:117. doi:10.1038/s41467-021-26478-3.

33. Xu Y, Yang Y, Zhang W, et al. High-throughput calculations of magnetic topological materials. *Nature*. 2020;586(7828):702-707. doi:10.1038/s41586-020-2837-0.
34. Bera S, Behera P, Venkatesh R, Ganesan V. Magnetotransport and thermal properties of microwave synthesized nanostructured Bi2Te3. *Journal of Applied Physics*. 2021;129(19):194304. doi:10.1063/5.0045126.
35. Witting IT, Eklund C, Roddick A, et al. The thermoelectric properties of bismuth telluride. *Advanced Electronic Materials*. 2019;5(2):1800904. doi:10.1002/aelm.201800904.
36. Cao T, Zhao X, Zhang Y, et al. Advances in bismuth-telluride-based thermoelectric devices: Progress and challenges. *eScience*. 2023; 3:100122. doi: 10.1016/j.esci.2023.100122.
37. Sarnet T, Macek J, Ziese M, et al. atomic layer deposition and characterization of Bi_2Te_3 thin films. *The Journal of Physical Chemistry A*. 2015;119(12):2298-2306. doi:10.1021/jp5063429.
38. Pandey L, Chandra B, Prakash P, et al. Topological transport properties of highly oriented Bi_2Te_3 thin film deposited by sputtering. *Journal of Physics: Condensed Matter*. 2023;35(12):355702. doi:10.1088/1361-648x/acd50a.
39. Le PH, Liu PT, Luo CW, Lin JY, Wu KH. Thickness-dependent magnetotransport properties and terahertz response of topological insulator Bi_2Te_3 thin films. *Journal of Alloys and Compounds*. 2017; 692:972-979. doi: 10.1016/j.jallcom.2016.09.109.
40. Weyrich C, Heider P, Hofer K, et al. Growth, characterization, and transport properties of ternary $(Bi_{1-x}Sb_x)_2Te_3$ topological insulator layers. *Journal of Physics: Condensed Matter*. 2016;28(49):495501. doi:10.1088/0953-8984/28/49/495501.
41. Pilidi A, Speliotis T, Litsardakis G. Structural and magnetotransport characterization of magnetron sputtered co-doped Bi_2Te_3 thin films. *Journal of Magnetism and Magnetic Materials*. 2020; 511:166971. doi: 10.1016/j.jmmm.2020.166971.
42. Liu CX, Zhang SC, Qi XL. The quantum anomalous Hall effect: Theory and experiment. *Annual Review of Condensed Matter Physics*. 2016; 7:301-321. doi:10.1146/annurev-conmatphys-031115-011417.
43. Serlin M, Noh J, Hovey K, et al. Intrinsic quantized anomalous Hall effect in a moiré heterostructure. *Science*. 2020;367(6481):900-903. doi:10.1126/science. aay5533.
44. Sharpe AP, Zhang Y, Lee JI, et al. Emergent ferromagnetism near three-quarters filling in twisted bilayer graphene. *Science*. 2019;365(6455):605-608. doi:10.1126/science. aaw3780.
45. Chen G, Wu S, He X, et al. Evidence of a gate-tunable Mott insulator in a trilayer graphene moiré superlattice. *Nature Physics*. 2019;15(3):237-241. doi:10.1038/s41567-018-0387-2.
46. Martin LW, Chu Y-H, Ramesh R. Advances in the growth and characterization of magnetic, ferroelectric, and multiferroic oxide thin films. *Mater Sci Eng R Rep*. 2010;68(4-6):89-133. doi: 10.1016/j.mser.2010.03.001.
47. Henzler M. Growth modes in homo- and heteroepitaxial growth. *Prog Surf Sci*. 1993;42(1-4):297-316. doi:10.1016/0079-6816(93)90077-9.
48. Tan C, Chen J, Wu XJ, et al. Epitaxial growth of hybrid nanostructures. *Nat Rev Mater*. 2018; 3:17089. doi:10.1038/natrevmats.2017.89.

49. Chambers SA. Epitaxial growth and properties of doped transition metal and complex oxide films. *Adv Mater*. 2010;22(2):219-248. doi:10.1002/adma.200901867.
50. Janarthanan B, Thirunavukkarasu C, Maruthamuthu S, et al. Basic deposition methods of thin films. *J Mol Struct*. 2021; 1241:130606. doi: 10.1016/j.molstruc.2021.130606.
51. Bailini A, Donati F, Zamboni M, et al. Pulsed laser deposition of Bi_2Te_3 thermoelectric films. *Appl Surf Sci*. 2007;254(4):1249-1254. doi: 10.1016/j.apsusc.2007.09.039.
52. Theerthagiri J, Karuppasamy K, Lee SJ, et al. Fundamentals and comprehensive insights on pulsed laser synthesis of advanced materials for diverse photo- and electrocatalytic applications. *Light Sci Appl*. 2022; 11:250. doi:10.1038/s41377-022-00904-7.
53. Christen HM, Eres G. Recent advances in pulsed-laser deposition of complex oxides. *J Phys Condens Matter*. 2008;20(26):264005. doi:10.1088/0953-8984/20/26/264005.
54. Wasa K, Kitabatake M, Adachi H. Thin film materials and devices. In: Wasa K, Kitabatake M, Adachi H, eds. *Thin Film Materials Technology*. William Andrew Publishing; 2004:1-16. doi:10.1016/B978-081551483-1.50002-2.
55. Concepción O, Pereira VM, Choa A, et al. The growth of Bi_2Te_3 topological insulator films: Physical vapor transport vs molecular beam epitaxy. *Mater Sci Semicond Process*. 2019; 101:61-66. doi: 10.1016/j.mssp.2019.05.025.
56. Zeng Z, Morgan TA, Fan D, et al. Molecular beam epitaxial growth of Bi_2Te_3 and Sb_2Te_3 topological insulators on GaAs (111) substrates: a potential route to fabricate topological insulator p-n junction. *AIP Adv*. 2013;3(7):072112. doi:10.1063/1.4815972.
57. Arthur JR. Molecular beam epitaxy. *Surf Sci*. 2002;500(1-3):189-217. doi:10.1016/S0039-6028(01)01525-4.
58. Depla D, Mahieu S, Greene JE. Sputter deposition processes. In: *Handbook of Deposition Technologies for Films and Coatings*. 3rd ed. Elsevier; 2010:253-296. doi:10.1016/b978-0-8155-2031-3.00005-3.
59. Ahmed A, Han S. Fabrication, micro-structure characteristics and transport properties of co-evaporated thin films of Bi_2Te_3 on AlN coated stainless steel foils. *Sci Rep*. 2021; 11:4041. doi:10.1038/s41598-021-83476-7.
60. Rawther AN, Rout U, Kumar DS, Ramanathan R, Mallik RC. Thermoelectric properties of sputter deposited Bi_2Te_3–PbTe multilayer thin films. *Physica B*. 2024; 673:415467. doi: 10.1016/j.physb.2023.415467.
61. Ning J, Martinez JC, Momand J, et al. Differences in Sb_2Te_3 growth by pulsed laser and sputter deposition. *Acta Mater*. 2020; 200:811-820. doi: 10.1016/j.actamat.2020.09.035.
62. Bergström J. Experimental characterization techniques. In: Bergström J, ed. *Mechanics of Solid Polymers*. William Andrew Publishing; 2015:19-114. doi:10.1016/B978-0-323-31150-2.00002-9.
63. Mohamed MA, Mohd Hir ZA, Wan Mokthar WNA, Osman NS. Features of metal oxide colloidal nanocrystal characterization. In: Thomas S, Sunny AT, Velayudhan P, eds. *Metal Oxides, Colloidal Metal Oxide Nanoparticles*. Elsevier; 2020:83-122. doi:10.1016/B978-0-12-813357-6.00008-5.
64. Harrington GF, Santiso J. Back-to-basics tutorial: X-ray diffraction of thin films. *J Electroceram*. 2021; 47:141-163. doi:10.1007/s10832-021-00263-6.

65. Shokrieh MM, Ghanei Mohammadi AR. Non-destructive testing (NDT) techniques in the measurement of residual stresses in composite materials: an overview. In: Shokrieh MM, ed. *Residual Stresses in Composite Materials*. Woodhead Publishing; 2014:58-75. doi:10.1533/9780857098597.1.58.
66. Yasaka M. X-ray thin-film measurement techniques. *Rigaku J*. 2010;26(2):1-9.
67. Joshua AM, Cheng G, Lau EV. Soft matter analysis via atomic force microscopy (AFM): A review. *Appl Surf Sci Adv*. 2023; 17:100448. doi: 10.1016/j.apsadv.2023.100448.
68. Greczynski G, Hultman L. X-ray photoelectron spectroscopy: Towards reliable binding energy referencing. *Prog Mater Sci*. 2020; 107:100591. doi: 10.1016/j.pmatsci.2019.100591.
69. Grinter DC, Thornton G. Characterization tools for ultrathin metal oxides. In: Wandelt K, ed. *Encyclopedia of Interfacial Chemistry*. Elsevier; 2018:62-85. doi:10.1016/B978-0-12-409547-2.12870-7. ISBN 9780128098943.
70. Nemcsics Á, Nagy Sz. Plausible quantum-mechanical interpretations of RHEED oscillation. *Vacuum*. 2012;86(6):620-622. doi: 10.1016/j.vacuum.2011.07.020.
71. Hernández-Calderón I. Epitaxial growth of thin films and quantum structures of II–VI visible-bandgap semiconductors. In: Henini M, ed. *Molecular Beam Epitaxy*. Elsevier; 2013:311-346. doi:10.1016/B978-0-12-387839-7.00014-2. ISBN 9780123878397.
72. W Becker. The turbomolecular pump, its design, operation and theory; calculation of the pumping speed for various gases and their dependence on the forepump. *Vacuum*. 1966;16(11):625-632. doi:10.1016/0042-207X (66)91425-4.
73. Audi M, de Simon M. Ion pumps. *Vacuum*. 1987;37(8-9):629-636. doi:10.1016/0042-207X (87)90048-0.
74. Hall LD. Ionic vacuum pumps. *Science*. 1958;128(3319):279-285. doi:10.1126/science.128.3319.279.
75. Weingartner HC, Kennedy SW. A review of modern vacuum pumps in electronics manufacturing. In: Marton L, ed. *Advances in Electronics and Electron Physics*. Vol 5. Academic Press; 1953:213-246. doi:10.1016/S0065-2539(08)60687-3. ISBN 9780120145058.
76. Chambers A. *Modern Vacuum Physics*. United Kingdom: CRC Press; 2004.
77. Bhattacharjee N, Mahalingam K, Fedorko A, et al. Effects of Crystalline Disorder on Interfacial and Magnetic Properties of Sputtered Topological Insulator/Ferromagnet Heterostructures. *ACS Appl Electron Mater*. 2022;4(9):4288-4297. doi:10.1021/acsaelm.2c00523.
78. Zou Q, Shang H, Huang D, et al. Bi2Te3-based flexible thermoelectric generator for wearable electronics. *Appl Phys Lett*. 2022;120(2):023903. doi:10.1063/5.0078389.
79. Guo Q-X, et al. Effects of post-annealing on crystalline and transport properties of Bi_2Te_3 thin films*. *Chinese Phys B*. 2021; 30:067307. doi:10.1088/1674-1056/abee6c.
80. Zhao Y-J, Zhou F. Synthesis, Evolution of Morphology, Transport Properties for Bi_2Te_3 Nanoplates. *Crystals*. 2022; 12(11):1668. https://doi.org/10.3390/cryst12111668
81. Gong T, Gao L, Kang L, et al. Ultrahigh power factor of sputtered nanocrystalline n-type Bi_2Te_3 thin film via vacancy defect modulation and Ti additives. *Adv Sci*. 2024;2403845. doi:10.1002/advs.202403845.

82. Wang W, Sun K, Wang C, et al. Transient THz study of phonon-assisted carrier scattering between bulk and surface states in Bi2Te3. *J Phys Chem C*. 2023;127(49):23778-23784. doi: 10.1021/acs.jpcc.3c06365.
83. Adam AM, Tolan M, Refaat AA, et al. Optical properties of thin Bi_2Te_3 films synthesized by different techniques. *Superlattices Microstruct*. 2021; 155:106909. doi: 10.1016/j.spmi.2021.106909.
84. Pilidi A, Speliotis Th, Litsardakis G. Structural and magnetotransport characterization of magnetron sputtered co-doped Bi_2Te_3 thin films. *J Magn Magn Mater*. 2020; 511:166971. doi: 10.1016/j.jmmm.2020.166971.
85. Ahmad M, Kodan N, Ghosh A, Mehta BR. The nature of 2D:3D SnS: Bi_2Te_3 interface and its effect on enhanced electrical and thermoelectric properties. *J Alloys Compd*. 2020; 847:156233. doi: 10.1016/j.jallcom.2020.156233.
86. Fan P, Li R, Chen Y-X, et al. High thermoelectric performance achieved in $Bi_{0.4}Sb_{1.6}Te_3$ films with high (00l) orientation via magnetron sputtering. *J Eur Ceram Soc*. 2020;40(12):4016-4021. doi: 10.1016/j.jeurceramsoc.2020.04.059
87. Kimberly TQ, Wang EYC, Navarro GD, et al. Into the void: Single nanopore in colloidally synthesized Bi_2Te_3 nanoplates with ultralow lattice thermal conductivity. *Chem Mater*. 2024;36(13):6618-6626. doi: 10.1021/acs.chemmater.4c01092.
88. Hansen F, Fucke R, Charvin T, et al. Direct deposition of $(Bi_xSb_{1-x})_2Te_3$ nanosheets on Si/SiO_2 substrates by chemical vapor transport. *Cryst Growth Des*. 2022;22(4):2354-2363. doi: 10.1021/acs.cgd.1c01446.
89. Zhang M, Liu W, Zhang C, et al. Thickness-dependent electronic transport induced by in situ transformation of point defects in MBE-grown Bi_2Te_3 thin films. *Appl Phys Lett*. 2020;117(15):153902. doi:10.1063/5.0025828.
90. He X, Guan T, Wang X, et al. Highly tunable electron transport in epitaxial topological insulator $(Bi_{1-x}Sb_x)_2Te_3$ thin films. *Appl Phys Lett*. 2012;101(12):123111. doi:10.1063/1.4754108.
91. Kumar B, Tiwary CS, Paek M-K, Paliwal M. Thermodynamic modelling of the ternary Bi-Ga-Te system for potential application in thermoelectric materials. *Calphad*. 2021; 74:102326. doi: 10.1016/j.calphad.2021.102326.

Appendix A:

A1. AFM measurements:

Figure A1.1 shows the AFM measurements for one of our first deposited sample of Bi_2Te_3. The legend of Figure A1.1 includes the recipe for this sample.

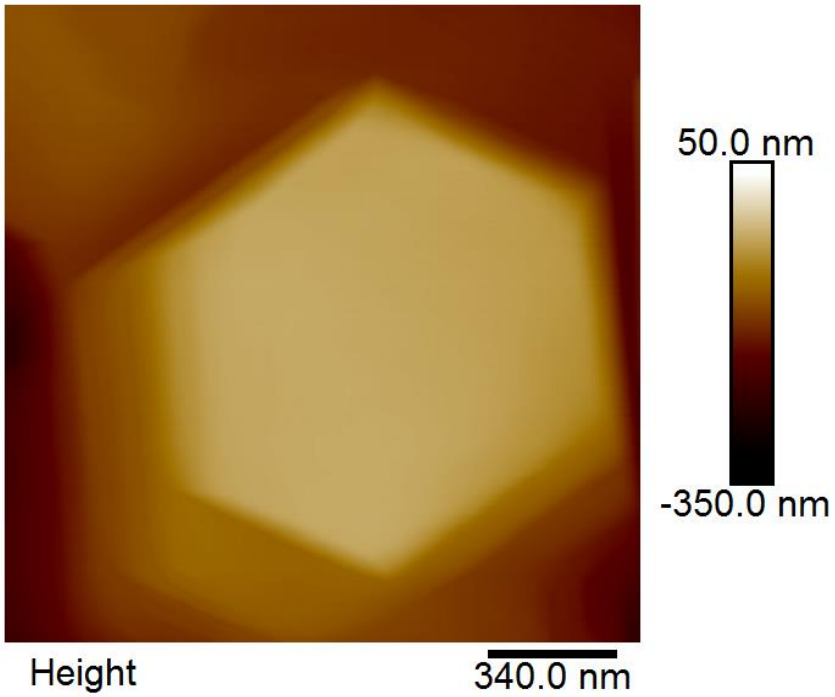

A 1.1: Island growth mode as can be seen from the scale on the right of the figure. The Bi cell temperature for this sample was at 665 °C with Te cell temperature at 412 °C. The stage temperature was at 220 °C and the growth duration was for 120 minutes accompanied by a post annealing process of 120 minutes

A2. Pole Figures

Figure A1.2 shows the pole figure for one of our Sb doped Bi_2Te_3 samples. The pole seen at the bottom, top right and top left of Figure A1.2 are due to the (015) plane. The intensity of these poles in figure A1.2 are much lower compared to pure Bi_2Te_3 samples indicating the role of doping in suppressing the (015) plane.

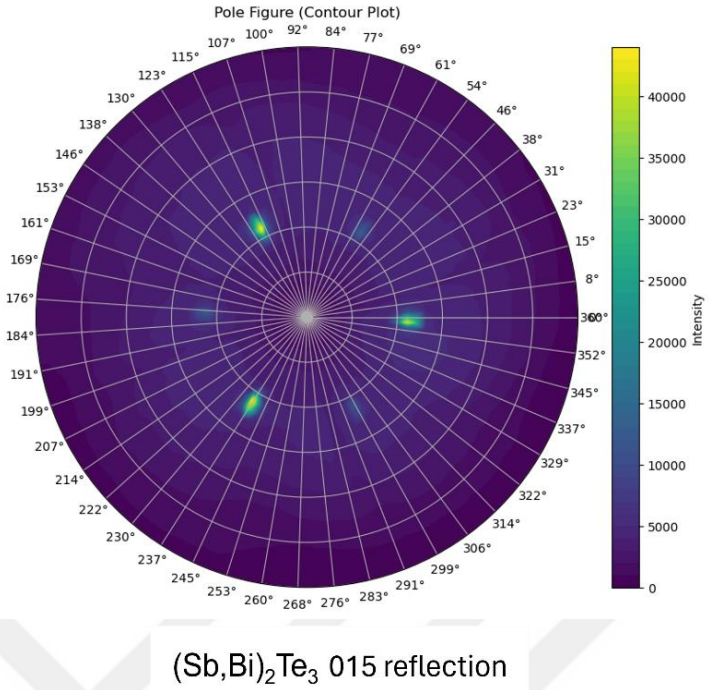

A 2.1: pole figure of doped sample from Figure A2.1.

A3. Raman Shifts

Figure A1.3 shows Raman measurements of 3 samples. One pure Bi_2Te_3 and two doped one at different Sb temperature. The rest of the parameters were the kept the same. The doped samples are the ones discussed in chapter 4. The shift in energy is an indication of successful doping.

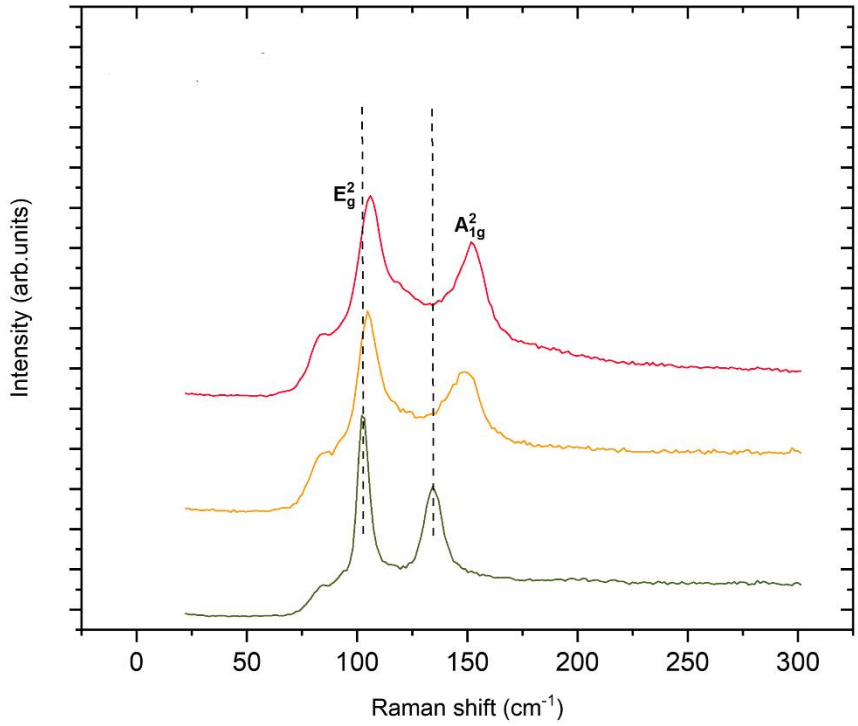

A 3.1: The red curve showcases the sample with Sb cell temperature at 450 °C while the yellow curve showcases the sample with Sb temperature at 455 °C. The green curve is a Bi_2Te_3 sample. All samples have the same parameters except the Sb addition and temperature change.